UoA Undergraduate Mechatronics Research Journal

UoA Undergraduate Mechatronics Research Journal

Preface

Welcome to the Undergraduate Research Journal of the Mechatronics Engineering Group at the University of Auckland's Department of Mechanical Engineering. This is the second volume of undergraduate papers describing some of the final year projects mechatronics engineering students have been working on. The journal offers undergraduates (contributions from postgraduate students are also welcome) the chance to present a summary of their achievements and will be published annually.

During their final year undergraduate students spend a quarter of their time on a research project of their choice. The research is carried out in teams of two and supervised by an academic from the Department. At the end of the two semesters students write a project report, give an oral presentation and prepare a poster. We invite students to submit a summary of their project to this Undergraduate Research Journal. We also intend publishing summer internship project work. All submitted manuscripts are internally peer-reviewed to ensure that only research of appropriate quality will be published in this journal.

We hope you enjoy reading about our students accomplishments and get an overview of the exciting domain of Mechatronics Engineering at the University of Auckland. We like to thank all reviewers and editors for their feedback and support.

Kean C. Aw and Enrico Haemmerle
Editor-in-Chief

Table of Contents

Composite Load Control for Wind Turbines

Jeffrey Kyle Lazaro, Maria Chakiath
The University of Auckland,
Department of Mechanical Engineering,
Mechatronics Engineering,
New Zealand
Email: jklazaro@gmail.com, chakiathm87@gmail.com

Abstract:
Wind turbines are sized according to their expected fatigue loads and any reduction in these would decrease costs and prolong working life. This article investigates a composite load controller for a wind turbine, with the goal of reducing tower fore-aft, low speed shaft (LSS) torsional, LSS tilt, and LSS yaw bending fatigue loads. The controller worked in conjunction with a baseline power controller and used individual pitch control to reduce asymmetric LSS vibrations. Simulations evaluated the composite design against the baseline controller alone, as well as single-input single-output (SISO) and multi-input multi-output (MIMO) architectures. Results showed significant mitigation of damage equivalent loads in tower fore-aft, and LSS tilt and yaw directions across all designs when compared to baseline. Little to no reduction in LSS torsional loads was achieved. It is concluded that active control can reduce structural fatigue and the composite setup achieves similar attenuation to SISO and MIMO controllers.

Keywords: *Wind turbine; fatigue load control; linear quadratic regulator; multi-blade coordinate transformation; individual pitch control*

1. Introduction

Wind turbines convert kinetic energy in the wind into mechanical energy, which is then used to generate electricity. A typical controller aims to maximise power capture and decrease structural loads by actuating generator torque (T_g) and blade pitch (θ). These traditional baseline controllers consist of a single-input single-output (SISO) proportional integral (PI) or proportional integral derivative (PID) algorithm that generates pitch commands from the input generator speed, with a torque command generated independently for variable-speed turbines [1].

Wind turbines are growing larger and active control to reduce structural fatigue is an important field. The aim of this project is to test the performance of a composite MIMO controller specifically aiming to minimise fatigue loads on a three-bladed horizontal axis wind turbine, which can reduce costs and increase operating life. The composite controller comprises of a MIMO linear quadratic regulator (LQR) to reduce fatigue loads and a baseline power controller for speed and torque management. The desired fatigue vibrations for attenuation are tower fore-aft, LSS tilt, LSS yaw, and LSS torsional bending moments. Comparisons are made to baseline alone, a design consisting of baseline with multiple SISO load controllers, and finally a design with a single MIMO controller. The particular turbine model considered in this project is rated at 5-MW with a hub height of 90 meters. For more information, refer to [1].

2. Power and Load Control

The power curve for a typical wind turbine is shown in Figure 1. In Region 1 the wind is not fast enough to overcome mechanical losses and the turbine remains off. Once cut-in has been reached, the goal of Region 2 is to maximise power capture through torque control. In Region 3, capturing any more power is no longer economical and the goal is to keep rotor speed at rated through pitch control. At cut-out the wind is too fast and the turbine is shut down.
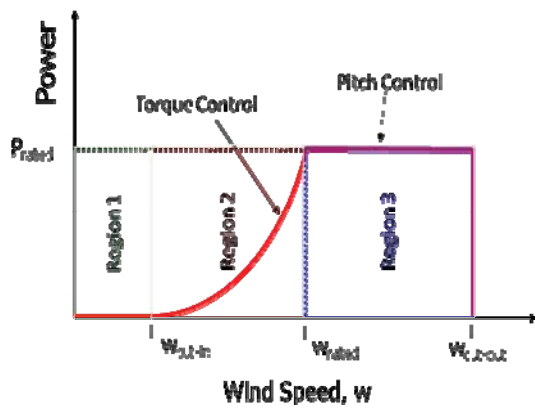

Figure 1. Power curve for a wind turbine

Pitching action involves rotating the blades about its longitudinal axis and in doing so, aerodynamic forces are influenced and the rotor speed is controlled. The rotor blades can be pitched collectively or individually to address symmetric (tower fore-aft) and asymmetric fatigue loads (shaft tilt and shaft yaw) respectively. Applying a torque on the generator primarily affects symmetric shaft loads (shaft torsional moment).

3. Composite Load Controller

The composite architecture consists of a MIMO controller for the fatigue loads and a baseline controller for power regulation (Figure 2). This design has two advantages. Firstly, the load reduction objectives can be emphasised in design and the controller is 'aware' of any coupling present. This is desirable so that the control actions do not overly conflict with each other. Secondly, transition between Regions 2 and 3 can be better handled by the power controller as it deals with integral wind-up. This occurs when the integral term of the PI pitch controller grows larger and larger in Region 2 (as the rotor speed will never reach rated) so once it becomes active in Region 3, the control action is incorrect. The PI pitch controller includes an integral reset to account for this, but in MIMO state-space designs this is not practical especially when state estimation is involved. In this project the wind files used for testing are not turbulent enough to include transition so this advantage of the composite design is not fully realised.
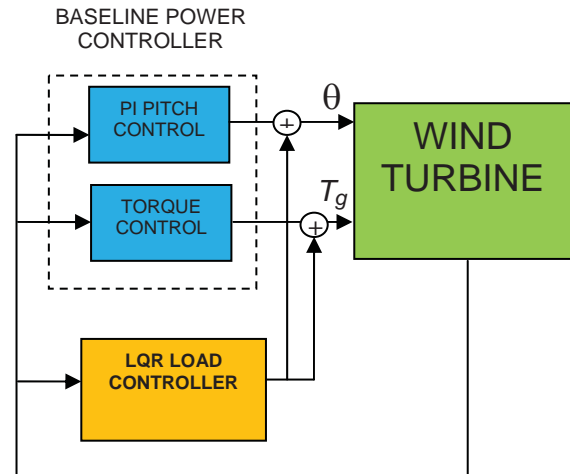

Figure 2. Composite controller diagram

The linear state-space model of the wind turbine has three degrees of freedom (tower fore-aft motion, generator angle, and LSS torsion) and is obtained numerically using FAST, an aero-elastic simulation code for wind turbines [2]. The state vector ($\underline{x}$) equation is related to the inputs ($\underline{u}$) and is of the form:

$$\Delta \underline{\dot{x}} = A(\psi)\Delta \underline{x} + B(\psi)\Delta \underline{u} \tag{1}$$

The model is highly periodic with rotor blade azimuth angle (ψ) and thus multi-blade coordinate transformation (MBC) is used to transform any dynamics in the

rotating frame to a fixed coordinate system [3]. This has the effect of reducing the periodicity of the state-space model and thus the matrices in equation (1) can be averaged to give:

$$\Delta \dot{x} = \bar{A}\Delta x + \bar{B}\Delta u \qquad (2)$$

The linear time invariant system is used to design an optimal full-state feedback (FSFB) controller using linear quadratic regulation. A characteristic cost function describes the balance between the conflicting objectives of state regulation and actuator usage and the solution that satisfies the FSFB control law is an LQR controller. Because two of the load measurements are not states (LSS yaw and tilt) these must be obtained using outputs from the turbine and the LQR cost function is augmented:

$$I = \int_0^t \left(y^T Q' y + u^T R u \right) dt \qquad (3\text{-}1)$$

$$Q = C^T Q' C \qquad (3\text{-}2)$$

In this way, the outputs can be regulated and the relationship between the familiar state weighting matrix Q and the augmented Q' that gives weightings to the outputs is shown in equation (3-2).

Weightings are only given to state velocities since the goal is to reduce back and forth motions that give rise to structural fatigue. Specifically, more emphasis is given to the tower fore-aft state velocity than shaft torsional velocity because the drive-train of the particular turbine model has high intrinsic damping [1]. This can be seen by two poles on the far left of the imaginary axis (not shown) while the tower fore-aft poles are only lightly damped [4].

With regards to input weightings, excessive torque commands for load attenuation conflict with power regulation and hence more importance is given to collective and individual pitch usage. By inspection of the

Bode plot of collective pitch to shaft tilt and yaw bending moments, it can be seen that collective pitch can affect asymmetric loads as well. This is due to the coupling that exists between the tower fore-aft and asymmetric shaft loads. However individual pitch usage still gives the best broad frequency control action as expected [4]. LQR tools in MATLAB are used to calculate the final gain matrix and this is made periodic by reverse MBC to generate individual pitch commands.

4.   Multiple SISO Controller

The SISO controller consists of three SISO loops (Figure 3) and is the model that considers the coupling between objectives the least as the control paths are synthesised without knowledge of each other. This of course runs the risk of clashing control actions.
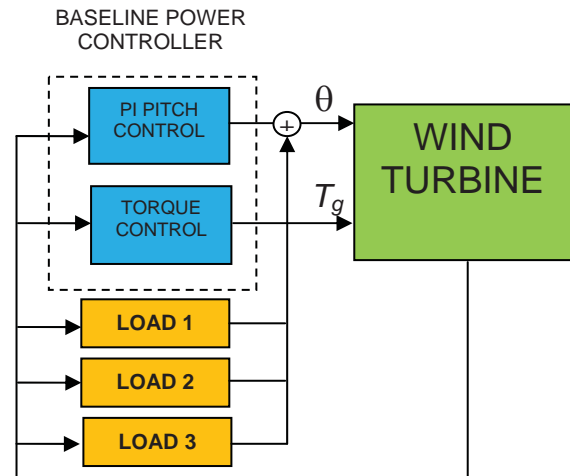
Figure 3. Multiple SISO controller diagram

The main advantage of SISO architectures is that classical design techniques can be used which are well known and less complex than state-space methods. Like the composite controller, individual pitch control (IPC) is used so that the three control paths take care of fatigue loads in the tower fore-aft, shaft tilt, and shaft yaw direction. The input measurements are fore-aft velocity, shaft tilt bending moment, and shaft yaw bending moment respectively. Shaft torsion is not

3

added as an objective because as explained earlier, the drive-train has high natural damping and this is also why less emphasis is on the shaft torsional state for the multivariable controllers. Note that the methods to design the load controller are those described by Bossanyi [5].

5. Single MIMO Controller

The main advantage of a single multivariable design is that load and speed objectives can be combined, thus reducing potential conflict between the control efforts. However torque control for power regulation is problematic and there can be issues with region transition due to integral wind-up. The creation of this controller is straightforward once the composite model has been designed. This is because they are identical except that the single MIMO controller now manages rotor speed through pitch control.

6. Results and Discussion

The designed controllers are tested using FAST to simulate the non-linear wind turbine with the three degrees of freedom considered. The wind files are created using TurbSim, a stochastic, full field, turbulent-wind simulator [6].

Five percent turbulent wind profiles including wind shear are used over a 600 second (10 minute) test period. For fair testing, the controller gains are tuned to achieve the same power and speed tracking as baseline with a steady wind velocity at the two operating points chosen. The root mean square (RMS) pitch rate shows how much control effort is being used and this is important because it gives a good indication of actuator usage. RMS power error is from the rated five megawatts. Note that the results have been normalised to baseline.

The performance metric for structural fatigue is damage equivalent loads (DEL) and this is calculated by taking the various frequency components of the load signal and finding the equivalent one hertz representation. Table 1 shows the results for above rated (Region 3) conditions.

Table 1. Results for above rated wind conditions

	SISO	Comp.	sMIMO
RMS Power Error	1.07	1.07	0.86
RMS Speed Error	1.07	1.07	0.93
RMS Pitch Rate	3.63	3.45	4.64
Tower FA DEL	0.50	0.51	0.36
Shaft Tor. DEL	1.00	1.00	0.99
Shaft Yaw DEL	0.94	0.92	0.91
Shaft Tilt DEQL	0.91	0.90	0.85

The RMS power and speed error for all models are close to baseline indicating fair testing. Tower fore-aft sees a large reduction in DEL of 50% for the SISO and composite designs and 64% for the single MIMO controller. Additionally, the single MIMO design achieves slightly more asymmetric shaft load attenuation. Given the higher pitch rate of this controller (also caused by speed regulation) this is expected. Shaft torsion sees little to no DEL reduction. Table 2 shows the results for below rated (Region 2) conditions.

Table 2. Results for below rated wind conditions

	SISO	Comp.
Mean Power Capture	0.99	1.00
RMS Pitch Rate	1.00	3.74
Tower FA DEL	0.62	0.61
Shaft Tor. DEL	1.00	1.02
Shaft Tilt DEL	0.91	0.91
Shaft Yaw DEL	0.95	0.93

In Region 2 the goal is to maximise power capture (speed and power will not be at rated) hence mean power capture is used as a performance metric. As shown, this is comparable in the SISO and composite designs. The single MIMO design is not considered because the pitch controller for power capture is unused in below rated conditions and thus it is identical to the composite model. Reductions in tower fore-aft DEL are close to 40% for both controllers, while asymmetric shaft loads sees modest decreases. For this condition the SISO model appears superior in having less

pitching action and 2% less shaft torsional fatigue. The 374% less pitching likely comes from the SISO controller emphasising collective over individual pitch actuation. Figure 4 shows the power spectral density plots of the loads for above rated turbulent conditions.
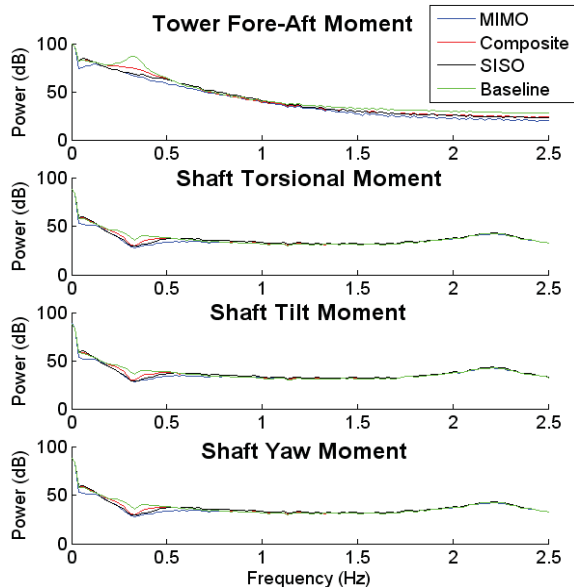

Figure 4. Power spectral density plots of the loads

The natural frequency of the tower fore-aft mode occurs at 0.33 Hz and the controllers are successful in reducing this resonant peak. On the other hand, the shaft natural frequency is at 2.2 Hz and this peak achieves little to no damping.

7.   Conclusions

- Active control is successful in reducing cyclic fatigue loads on a wind turbine. The composite, SISO, and single MIMO designs all showed similar attenuations of up to 50% tower fore-aft DEL and up to 10% asymmetric shaft DEL. This was consistent in above and below rated conditions with turbulent wind. In constant wind, reductions of around 50% in asymmetric shaft DEL were seen.
- Individual pitch control is useful for mitigating asymmetric shaft loads. Collective action also has a large effect

on these due to the strong coupling with the tower fore-aft mode.
- Shaft torsional DEL had little to no reductions across the three load controllers in all test conditions as this particular mode had high intrinsic damping and was not easily excited by the wind. Actuating generator torque excessively also interfered with power regulation hence the controllers were tuned to emphasise the other states.
- The main advantage of the SISO controller is that it is easy to understand and utilises well known classical design techniques. Region transition is handled as well. The disadvantage of this design is that creating multiple control loops can create unnecessary conflicts with the competing regulation objectives.
- The main advantage of the composite design is that it incorporates coupling between the load objectives and region transition is handled. It requires more complex design methods however.
- The main advantage of the single MIMO design is that it handles the coupling between speed and load regulation goals and hence is suitable for multivariable problems such as wind turbine control. This is at the cost of being the most complex design and there are potential problems with region transition. Moreover, torque control for managing power capture can prove difficult.
- All three designs have their merits and it is up to the designer to assess which model would be appropriate. The main attraction of using multivariable control is that the connection between objectives is taken care of and in more complex scenarios (with more degrees of freedom) this may be advantageous.

Acknowledgements

References

[1]   Jonkman, J.M. (2007) Dynamics Modeling and Loads Analysis of an Offshore Floating Wind Turbine. PhD Thesis, University of Colorado.

[2]   Jonkman, J.M. and Marshall, L.B. (2005) FAST User's Guide. Technical Report NREL/EL-500-38230, National Renewable Energy Laboratory, Colorado.

[3]   Bir, G. (2008). *Multiblade Coordinate Transformation and Its Application to Wind Turbine Analysis*. 2008 ASME Wind Energy Symposium, Reno, Nevada.

[4]   Lazaro, J.K. (2009) *Composite Load Controller for Wind Turbines*. Part IV project report, 2009-MT21. Mechanical Engineering Department, University of Auckland.

[5]   Bossanyi, E.A. and Hassan, G. (2003) Individual Blade Pitch Control for Load Reduction. *Wind Energy*, **6**, pp 119-128.

[6]   Jonkman, J.M. and Buhl, M.L. (2008) TurbSim User's Guide for Version 1.40. Technical Report NREL/TP-xxx, National Renewable Energy Laboratory, Colorado.

Flexible Impact Sensor Using IPMC

S.C. Fang, H.H. Chen
The University of Auckland,
Department of Mechanical Engineering,
Mechatronics Engineering,
New Zealand

Abstract:
Ionic Polymer Metallic Composite (IPMC) sensors offer several advantages over conventional sensors; advantages such as flexibility and durability are useful in the area of impact sensing. The aim is to demonstrate the concept of using IPMC for impact sensing. An impact tester was developed based on the IPMC strip in a cantilever configuration. A mathematical model was developed from experimental date to predict impact energy based on the slope of the voltage response.

Keywords: *IPMC, impact sensor*

1. Introduction

Although still in research stage, the potential applications of IPMC range from artificial muscle, micro-pumps to bio-mimetic robots [1, 2]. Majority of the research focus on developing IPMC as actuators, only a small portion of research investigate its potential in sensing applications. However, IPMC does have several advantages over other smart materials in the field of sensing. One main advantage IPMC is that it is a passive sensor; therefore requires no external power supply. The flexibility and durability of polymer also makes IPMC more attractive in applications where large and continuous deformation is expected. It is also able to operate in environment with excessive moisture, although the sensor response could become more unpredictable. Furthermore, IPMC is easy to manufacture because it has simple structure, thus can be a potentially cheap solution if mass manufactured [3]. The combination of these properties makes IPMC useful in the area of impact sensing
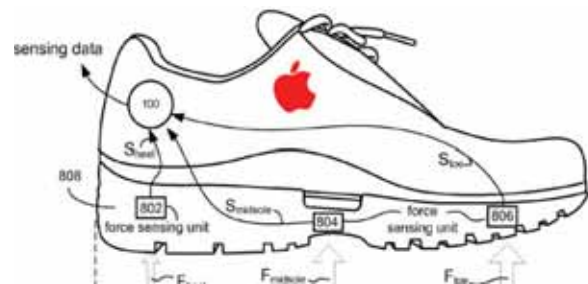

Figure1. Apple's next generation shoe with force sensors and GPS [4].

where large force and deformation are expected. One distinct advantage the IPMC has over conventional strain gauge is that it can be embedded into a soft material whereas strain gauges are typically mounted on hard surfaces. Therefore IPMC may be useful in sports science applications where the sensing surface is in contact with human body. Figure 1 shows the embodiment of force sensor inside the heel of a shoe to determine the distribution of force.

The aim of the project is to investigate the potential of IPMC in a practical impact

sensing application. The chosen application is the implementation of IPMC sensor in the heel of a shoe where the IPMC is embodied inside a soft material. The research will be a proof of concept that IPMC has the potential to be used in similar impact sensing applications.

2.   Experimental Set-up

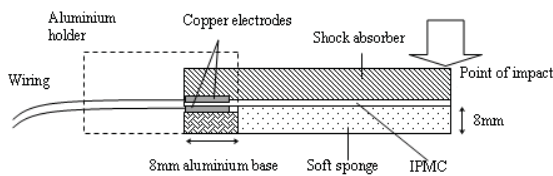The sensor is constructed with the IPMC sandwiched between two soft materials as shown in Figure 2.

Figure 2. An IPMC-based impact sensor

An experimental rig was constructed to conduct the impact testing, where the height of the drop mass determines the impact energy. Two light sensors near the end of the impact sensor is used to determine the velocity of the drop mass; hence the kinetic energy which is also the impact energy (Figure 3).

Figure 3. An impact tester

The peak of the voltage spike from the IPMC is recorded as this can be correlated to the IPMC bending speed which in turn

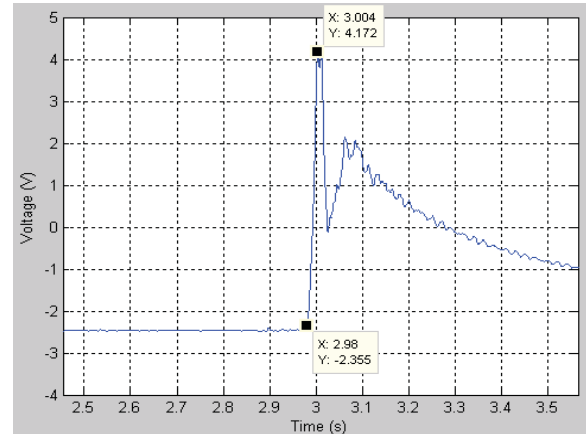correlated to the impact energy (See Figure 4).

Figure 4. A voltage response from the impact sensor

3.   Experimental Results

The peak of the voltage spike versus the impact energy is shown in Figure 5.
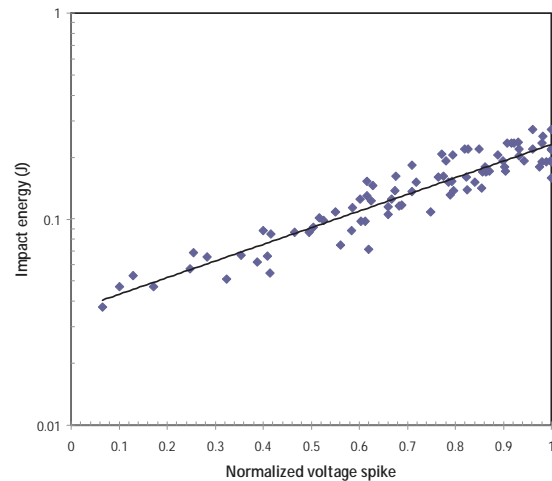

Figure 5. The Voltage spike versus impact energy

Figure 4 shows that there is an exponential relationship between the peak of the voltage spike and the impact energy with a relationship of $y = 0.0358e^{1.8601x}$ (where y - impact energy and x - the peak of the normalized voltage spike)

4.   Discussion and Conclusion

This project has demonstrated that the IPMC has the potential as an impact sensor. The

gradient of the voltage spike can be used to determine the impact energy. At this point of time, the mathematical model that was developed from the experimental data is based on limited range of impact energy (i.e. from 0.05J to 0.15J). However, it is believed that a higher impact energy measurement range can be achieved with different sandwiching materials.

References

[1] Kim K. J., S. Tadokoro (2007) *Electroactive Polymers for Robotics Applications: Artificial Muscles and Sensors,* Springer-Verlag London Ltd, London, 37-49

[2] Reece P. L. (2007) Smart Ionic Polymer-Metal Composites Design and Their Applications: An IPMC-driven ZNMF Pump with a Slot, *Progress in Smart materials and Structures, Nova Science Publishers*, New York, 92 – 110

[3] Bharti V., Bar-Cohen Y., Cheng Z. Y., Zhang Q., Madden J. (2005) *Electroresponsive Polymers and Their Applications*, 889, A Cost-Effective Fabrication Method for Ionic Polymer-Metal Composites, Material Research Society, US, 139-143

[4] Diaz J., Apple's Next-Gen Running Shoe Has Force Sensors, GPS Support, Retrieved Sept. 02, 2009 from http://gizmodo.com/5048363/apples-next+gen-running-shoe-has-force-sensors-gps-support

Improvement in Sensor Accuracy and Path Tracking of Autonomous Ground Vehicle

Chung-Che Wei, Lik Hang Andy Lee
The University of Auckland,
Department of Mechanical Engineering,
Mechatronics Engineering,
New Zealand

Abstract:
An Autonomous Ground Vehicle (AGV) is a vehicle which is specifically designed to auto-guide itself between designated waypoints without any human intervention. Such a vehicle has been developed at the University of Auckland, and it consists of three sensors; Global Positioning System (GPS) receiver, electronic compass and Inertial Measurement Unit (IMU). A Kalman Filter was used to remove noises and fluctuations that exist in the sensor outputs. An Altera DE2 Development Board, which includes an onboard Field Programmable Gate Array (FPGA) was used as the processor for vehicle control. The Dead Reckoning algorithm was implemented for vehicle path navigation, and test results have shown that the AGV performance has a maximum deviation of 1 metre for straight line path, and 2 metres for triangular path.

Keywords: *Autonomous Ground Vehicle; FPGA; Kalman Filter; Path Tracking*

1. Introduction

An Autonomous Ground Vehicle (AGV) is a vehicle which is specifically designed to auto-guide itself between designated waypoints. By using a combination of sensors and processors, an AGV is able to retrieve information from its environment and localize itself. Once the vehicle has obtained its current position and orientation (known as localization), a path tracking algorithm is executed to ensure the AGV follows the desired path (path tracking) with minimal deviation.

The Mechatronics Group at the University of Auckland (UoA) has been working extensively on a GPS-guided low-cost AGV over the past 4 years. The AGV has three onboard sensors; Global Positioning System (GPS) receiver, electronic compass and Inertia Measurement Unit (IMU).

The most recent improvement to the AGV, conducted in 2008 stabilized of the accelerometer output and incorporated an Altera DE2 Development Board as the vehicle controller. However, the current navigation ability of the AGV remains unsatisfactory.

Therefore, the main goal of this project is to further improve the AGV's localization and path tracking ability by modifying and improving the existing Kalman Filter as well as implementing and evaluating the Dead Reckoning path-tracking algorithm.

2. AGV System Overview

The AGV executes the navigation control by utilizing the Navman 1240 GPS receiver, Dinsmore 1252 Electronic Compass and Inertia Measurement Unit. Each sensor has their own driver circuits, and powered from

a Distribution Board. Apart from power distribution, the Distribution Board also acts as an intermediate interface where sensor data can be delivered to the FPGA control via ribbon cables. The raw sensor readings then undergo Kalman Filtering in order to remove the sensor noise as much as possible, and thus produce an accurate localization of the AGV. With these filtered data, path tracking algorithms can be accurately executed to give the necessary motor control information, which is used to steer the AGV along the desired path. An overview of the AGV system can be seen in Figure 1 below.
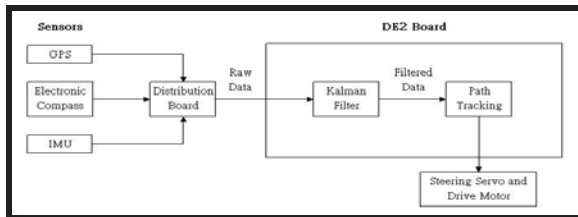

Figure 1. AGV system overview

3. Vehicle Hardware

Navman GPS1240 Receiver
The Navman GPS1240 antenna was used to determine the AGV's current location by communicating with satellites orbiting around the Earth. It is able to provide an accuracy of 10m, with an update frequency of 1Hz [1]. The GPS receiver sends out a series of NMEA data strings to the FPGA via the RS-232 serial port.

Dinsmore 1252 Electronic Compass
The electronic compass produces a sine and a cosine shaped voltage outputs which are be used to interpret the orientation of the compass [2], and thus the heading of the AGV. These analogue signals are converted into their 8-bit digital counterpart by using two Analogue-to-Digital Converters (ADC), one for each wave.

Inertia Measurement Unit
The IMU comprises of an ADXRS150EB gyroscope and ADXL213EB dual axis accelerometer. The gyroscope is an angular rate sensor which outputs an analogue signal which is proportional to angular rate about the axis normal to the top surface of the package. The accelerometer produces a Pulse Width Modulation (PWM) signal that is proportional to the magnitude and direction of angular acceleration [3].

Altera DE2 Development and Education Board
The Altera DE2 Board is an excellent system for implementing logic circuits and creating complex digital systems. One of the main reasons for using the DE2 board is the onboard FPGA. The FPGA allows great flexibility, as logic elements and circuitries can be implemented and reconfigured at any given time.

4. Kalman Filter

The Kalman Filter is an efficient recursive filter used to estimate the state of a linear dynamic system from a series of noisy measurements. Based on the estimated state from the previous time step and the current measurement, the current state can be computed. Therefore, by passing sensor outputs obtained from the GPS receiver, electronic compass and IMU through the Kalman Filter, a more accurate measurement of the AGV's current position and orientation can be collected. With this information, the AGV path tracking algorithm is able to steer and allow the AGV to follow the path more precisely.
In 2007, an 11-state Kalman Filter was implemented to include states of vehicle position, velocity, orientation, angular velocity and acceleration. These 11 states would give a complete representation of the vehicle kinematics as well as accounting

drift errors that accumulated over time. Noise covariance matrices, Q and R, were chosen through the conjunction of trial and error and sensor characterization.

Modifications were made to the Kalman Filter this year to improve the GPS and compass output performance. In order to reduce the large inaccuracy and noise present in the GPS signal, values correlating to the longitude and latitude in the measurement noise covariance matrix R were increased from 0.01 to 1000 to give less weighting to these noisy measurements. As the system is non-linear and complex, the weightings were tuned through trial and error, until a reasonable filtering result with a maximum error of 2m is achieved, as shown in Figure 2.
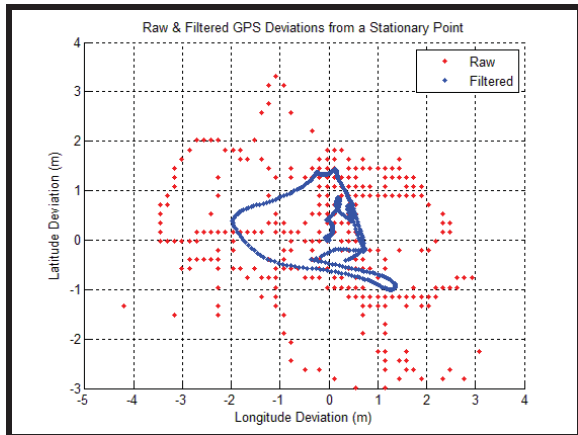

Figure 2. Raw and filtered GPS data measured from a stationary point

The compass provides an accurate stationary reading of a maximum error of 3°, however large signal spikes were present when the vehicle is in motion. The measurement noise matrix R was again modified to compensate for this issue and to improve the accuracy of the compass. This time, as the compass is much more reliable than the GPS, the value inside the R matrix was reduced from 0.01 to 0.005 to give more credibility to the measurements received from the compass. As seen in Figure 3, the

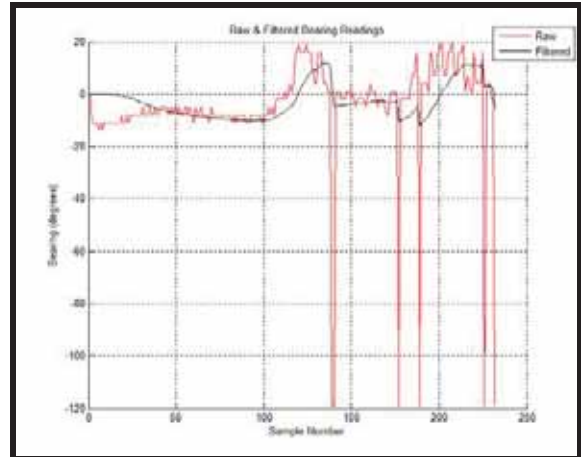spikes were filtered and a much more stable output was obtained.

Figure 3. Raw and filtered electronic compass data during motion

5.   Path Tracking – Dead Reckoning

Dead Reckoning is a path tracking method that does not rely on the current position of the AGV to execute path tracking. Instead it relies mostly on the orientation of the AGV. Since a standard way to implement the Dead Reckoning algorithm does not exist, it was therefore developed from scratch in the project. In this project the Dead Reckoning algorithm estimates the current position of the AGV by using the previous estimated position and its velocity.

Two separate co-ordinate systems, namely the world and vehicle co-ordinate systems (Figure 4) are used. The world co-ordinate system is defined so that x-axis points to the North and the y-axis points to the East, with an angle measured in clockwise direction being positive. The origin of the world co-ordinate system is the initial position of the AGV. The vehicle co-ordinate system is defined so that its origin is fixed on the centre of the AGV's rear axle with the x-axis pointing to the front of the AGV and the y-axis pointing to the right of the AGV, forming a right angle in between the two axes.
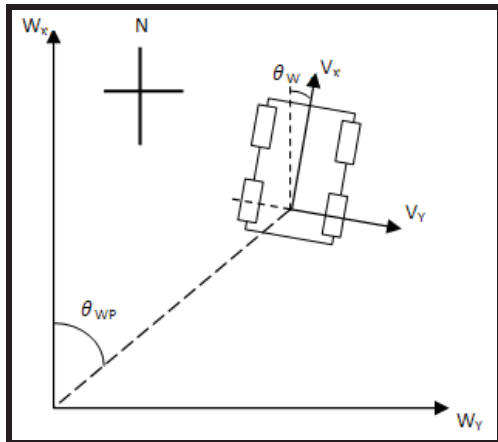
Figure 4. Co-ordinate systems used for Dead Reckoning

General Flow of Algorithm

Step 1 – Finding Separation
Separation is determined by calculating the perpendicular distance between the estimated position of the AGV and the path. A separation of bigger than 0.7 m is regarded as outside the path and varying this threshold value will change the tolerated path width. It will also affect how often maximum turning radius triggers as the AGV will turn with a maximum radius if it is outside the path.

Step 2 – Steering Decisions
The decision of how the steering is performed depends on the separation between the AGV and the path. If the AGV is not within the path, the AGV is steered towards the path with the minimum turning radius of 1.2m. If it is within the path the AGV is steered with a turning radius calculated using equation 1.

$$R_{turning} = \frac{1}{k \times \theta_{Diff}} \qquad (1)$$

Where $\theta_{Diff} = \theta_{WP} - \theta_{W}$

When the AGV is within the path and parallel with the path, the turning radius is arbitrarily set to 140 m in order to control

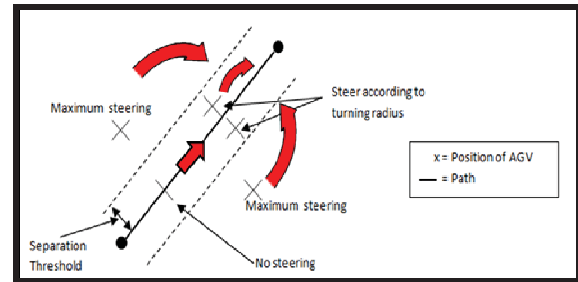the AGV to move straight. These conditions are summarised in Figure 5 below:

Figure 5. Illustration for Steering Decisions

6. Real World Testing

The vehicle was tested on straight line and triangular paths in order to examine the overall performance of the vehicle. A value of 0.7 m is used as separation threshold. The straight line path was used in order to test the ability of the vehicle to orientate in a straight line. This test was required to determine whether oscillations along a path were reduced. The triangular path was the formal test for the performance of the Dead Reckoning algorithm as the vehicle was required to navigate around corners.

7. Results and Discussion

Test Path 1 – Straight Line Path
The AGV offers a very reliable path tracking ability when tested over a straight line path such as the one shown in Figure 6 (dash lines on the graph indicate the separation threshold). This gives an indication that the Kalman Filter must has been successfully implemented and tuned to provide a better vehicle navigation. The deviation of the actual path from the desired path was also reduced from previous year's result of 2 m to 1 m.
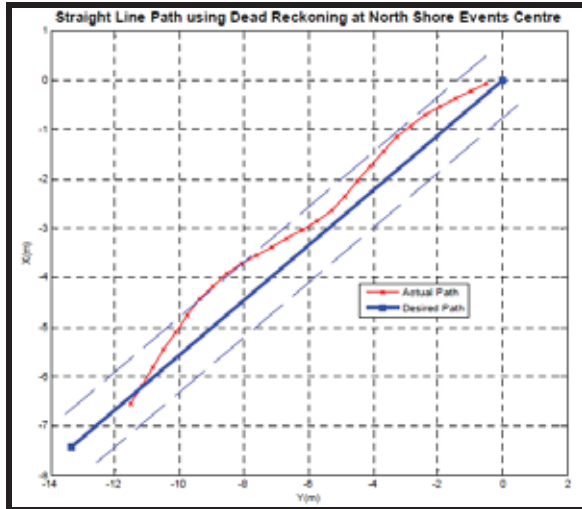
Figure 6. Performance of Dead Reckoning with Straight Line Paths

Figure 7. Performance of Dead Reckoning with Triangular Path

Test Path 2 – Triangular Path

Due to the undesired "delayed response" from the Kalman Filter, which is the time required by the filter to process and output the filtered readings; raw sensor data were used during triangular path testing. Figure 7 shows the result of path tracking performance for a triangular path. The estimated position calculated during navigation from origin to waypoint '1' was accurate and it is shown by the smooth path. However, the turning rate of the AGV was slow and it is represented by the large arc after waypoint '1' is reached. It is deduced that the slow sampling rate of the Kalman Filter is the main reason for the slow turning rate. Between waypoint '1' and waypoint '2' the vehicle appeared to be navigating with big oscillations and cannot settle onto the path. However, from real life observation, only a maximum overshoot of 2 metres was present throughout the entire testing.
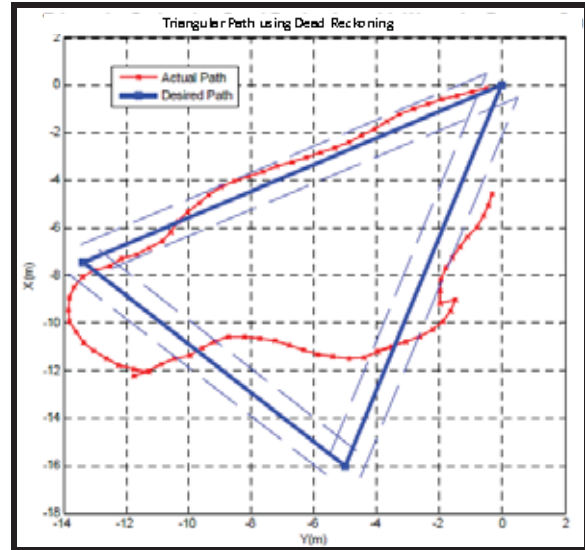
8. Conclusion

Sensor outputs from the GPS receiver and electronic compass were improved by modifying the Kalman Filter parameter.

With the implementation of the Dead Reckoning algorithm, the AGV is able to follow straight line paths using Kalman filtered data with a maximum deviation of 1 m and with almost no oscillation. It also presents a reasonably accurate path tracking performance when following a triangular path using raw sensor readings. Waypoints can be correctly reached and the vehicle is capable of trailing the desired path with small oscillations, and with a maximum deviation of 2 m.

Acknowledgements

References

[1] *Marine Electronics. Navman.* Retrieved June 6, 2009 from www.navmanmarine.net/upload/Marine/.../plastimo_07_eng.pdf

[2] *Dinsmore Sensor Information.* The Robson Company, Inc. Retrieved May 17, 2009, from http://www.jelu.se/shop/pdf/sensor%20information.pdf

[3] Analog Devices, (2004), ADXL213 Dual Axis Accelerometer Specification Sheet, Norwood,Massachusetts

Development of a Low-Cost Print-Head for OTFT Printer

Zhixiang (John) He, Jun (David) Jiang
The University of Auckland,
Department of Mechanical Engineering,
Mechatronics Engineering,
New Zealand

Abstract:
Organic Thin Film Transistor (OTFT), which is based on organic materials, has the capability to cover larger areas and compete in applications requiring structural flexibility compared to traditional TFT. In the past two years, the HP 1120C printer has been modified to provide dual-axes motion and a prototype print-head ink injection mechanism has been designed and constructed. This year, the ink injection mechanism was further improved by designing a new compressed spring system to provide the required force and was integrated with the existing structure. The injection mechanism was improved by using a new diaphragm seal. The two electronic circuit boards have been integrated into one. A control algorithm was developed to allow the system to actuate at different rates. The overall print-head mass has been reduced by 45% and the resolution of the system was improved to dispense at an average volume of 20nL.

Keywords: *organic thin film transistor; OTFT printer; injection mechanism; compressed spring*

1. Introduction

Thin Film Transistor (TFT) is a special type of field-effect transistor which is made by deposition of thin films of a semiconductor active layer over a supporting substrate. TFTs have been playing an integral role in the manufacturing of LCD screens. In recent years, there have been an increasing number of research and development into an alternative - Organic Thin Film Transistor (OTFT). OTFT have gained the public attention for its potential to dramatically reduce the fabricating cost for large-area electronics. It also has the capability to cover larger areas and compete in applications that require structural flexibility.

There are a number of methods of manufacturing OTFT including spin coating, mist coating or vapour deposition used for layering and photolithography for patterning. [1] Among the various methods, printing is a particularly attractive production process for users because it is low cost, applicable to large-area processing and compatible with flexible substrates. Printing also allows a drop-on-demand process, which gives user flexibility to control the film's area. Printing provides a route to high-speed, high-resolution and large-area OTFT manufacturing. Printing also reduces process steps and eliminates etching procedure. [2] However, the current industrial OTFT printer normally costs around NZ$35,000 and hence, a low-cost printing solution is desired as the University of Auckland wishes to further this research into OTFTs printing application in the future.

2.   Mechanical Improvements

Compressed Spring System

The compressed spring system is chosen to be the final design for the new force supplying system. The spring gets compressed when it sits on top of the syringe plunger. The expected maximum displacement of the spring will be less than 10mm because the maximum displacement usage of liquid is approximately 1mL for a typical OTFT printing. In other words, the spring needs to be relatively soft so that it gives about 20N force without having too large a compression force. The diameter of the syringe plunger is approximately 16mm. In order to save space and load, the spring needs to be as small as possible while it also meets the requirements.

Spring Cover Design

In order to save time and achieve simplify the overall system, the spring cover structure was designed and built based on the existing system structure. Minimum modification and cost are desired for the system. The spring cover was designed to fix the spring onto the syringe to prevent sideways movement while keeping it as compact as possible.

The spring cover for the compressed spring system was built on the top of two structural beams. Two 6mm holes were drilled into the beams to allow the bolts to slide through and fixing the spring cover onto the two beams. The spring cover was manufactured from rapid prototyping using ABS material. The ABS material is very tough and resilient. It has good chemical resistance and is non-toxic. The ABS material also allows the spring to be force-fitted onto the housing structure.

Figure 1 shows the integrated system: a U-shape rectangular block design with a cylindrical protrusion in the centre for holding the spring. The block has two long legs with holes into which bolt can be inserted through.
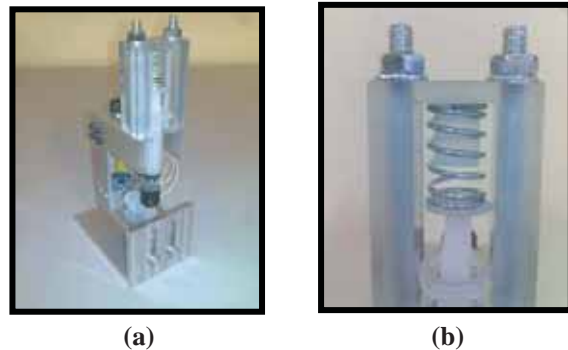

| (a) | (b) |

Figure 1. a) Integrated compressed spring system b) close up view

Diaphragm Seal System

The diaphragm seal used last year was not able to handle a high pressure because the elastic film was too thin to tolerate a large pressure. With all other exits blocked and high pressure applied, the flexible chamber of the diaphragm seal expands to an unacceptable size. In several occasions, the high pressure in the chamber forces the needle to move up without being actuated. In addition, the diaphragm seal does not return to its original flat state when the applied pressure is released because the diaphragm wall does not give enough elastic force to push the liquid back into the channel. In other words, the applied force makes the existing diaphragm seal go beyond its elastic limit and plastic deformation occurs. By using the compressed spring system, which applies a variable pressure, the existing thin and small diaphragm seal potentially has a higher chance of failing. Thus there is a need to improve the diaphragm seal to be more robust. A special bicycle tyre rubber is tested for the diaphragm seal. The rubber is strong and chemical resistant. However, the rubber is proven to be too thick to be installed in the existing structure. It is also so robust that it does not allow much deformation or expansion under pressure,

which may force the needle to move up without being actuated, forming bubbles at the tip of the nozzle valve. The diaphragm seal is replaced by the Pam's silver lined rubber gloves. The glove is made from premium Latex rubber and is nitrile blended for better organic material resistance. It is more durable than the current diaphragm seal. It is robust enough so that the material does not exceed its elastic limit when the pressure is applied while it allows a reasonable elastic deformation.

3.   Electronic Improvements

The power supply from the HP 1120C generates a DC voltage of 19V while the solenoid actuator operates at voltages ranging from 3.0V to 9.5V. Thus the voltage generated by the printer is required to be regulated down to drive the solenoid actuator.
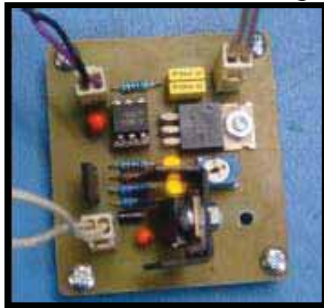

Figure 2. Control circuit PCB

In order to give a better flexibility for the solenoid in terms of different power ratings, the fixed 1k-ohm resistor was changed to a variable resistor.

The temperature of the voltage regulator increases during the actuation of the solenoid, especially at high duty cycle. High temperature influences the actuations of the solenoid and thus the operation of the liquid injection. Therefore apart from making the regulator operate at a low duty cycle during testing, a less temperature sensitive voltage regulator is chosen with a heat sink installed. The actuator driver circuit and power regulator circuit were combined into one printed circuit board (PCB), as shown in Figure 2, so that the overall system is more compact for easier integration with the printer.

4.   Software Improvements

In order to achieve a relatively constant dispensing volume for a compressed spring system, a new actuation algorithm needs to be developed. The new control software has to be capable of adjusting its rate of actuation according to different initial liquid levels. In other words, the change in spring force due to the varying displacement of the spring is compensated by the controlling program developed in C++. The system will have a higher actuation rate when there is less amount of liquid in the syringe.

A graphical user interface (GUI) based on MFC was developed and improved. The GUI allows the user to select of operation mode: automatic or manual mode. The duration of actuation, duty cycle and number of actuation can be adjusted in the GUI. The total number of actuation and initial liquid level are displayed in the GUI platform as well. This provides the user with an excellent platform for testing with all the controlling parameters that can be easily changed.

The timing control such as the duration of actuation is achieved by using the internal clocking of the computer. In the Mechatronics Laboratory, it is determined that the internal clocking of the computer has an accuracy error of approximately 20% compared to actual set time. A calibration process of the internal clocking has been included in the software for more accurate control.

The controlling algorithm has been improved so that there are two operation modes for the actuation of the print-head: manual and automatic mode. In manual operation mode, all the controlling parameters can be adjusted manually according to user's requirement. The switching on/off is controlled by the user as well. The manual operation mode is convenient for conducting tests before actual application and it is suitable for customized

application at times. In automatic operation mode, the controlling parameters are adjusted within the software and only the number of actuations is set manually. The adjustment is achieved by implementing the relationship of the liquid level and dispensing volume which is determined in experiments. The default duty cycle is set to be 5% for the automatic mode. The duration of actuation changes as the liquid level inside the syringe changes. The durations of each actuation are all set to be multiples of 2ms. The program will be automatically paused when it reaches the total number of actuation that the user pre-sets. The automatic mode assumes the user fills up the syringe to an initial level of 1.2mL each time before actuation.

5. Experiment Set-up

The compressed spring supplies a variable force to the syringe top at different displacement levels thus varying pressure will be applied to the system. The relationship between the liquid level and its corresponding dispensing volume needs to be estimated so that it can be implemented in the software control algorithm. In order to determine this relationship, experiments and tests are conducted. Because of the fixed height of the U-shape spring cover, the pressure applied to the system is only dependent on the fluid level of the reservoir syringe. The dispensed volume can be calculated by measuring the weight of the dispensing liquid if the density of the fluid is known.

In actual application, the print-head system is supposed to work with chloroform as dispensing organic material. However, the current print-head prototype is not suitable for the usage of organic material yet due to the material used for the print-head prototype and the syringe. Therefore water is used for testing the performance of the system instead of chloroform. Water is

about ten times more viscous than the chloroform. The vaporization temperature of chloroform is about four degrees lower than water. It indicates that the testing results may not be very accurate due to the difference in properties between the testing liquid water and actual dispensing material chloroform. The full set up is shown in Figure 3.
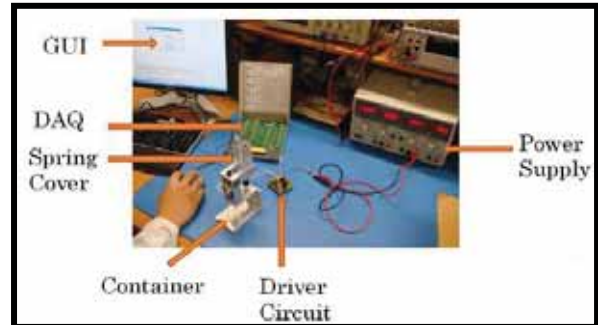

Figure 3. Experiment set-up

6. Results and Discussion

Effect of Different Actuation

The syringe was filled up to a predefined initial level of 1.4mL so that the initial pressure is maintained. Measurements were then recorded for different duration of actuation and the maximum number of cycles was determined. The first sharp increase in the curve shows the change from 2ms to 4ms while the second and third dramatic increase indicate the actuation duration change from 4ms to 6ms and 6ms to 8ms respectively. Results have shown that for a given fixed initial liquid level, the dispensing volume increases as the duration of actuation increases. The negativity was mainly due to the evaporation effect becoming a dominant factor for measurements at the later stage at a low actuation rate.

Effect of Different Initial Liquid Level

The initial liquid level of the syringe was changed and measurements were taken. Their minimum duration of actuation was set for the running of 2,000 cycles so that

Figure 4 Deposition Volume for Different Conditions

the minimum dispensing volume is measured for that initial particular liquid level. It is shown that the lower the initial liquid level, the smaller the deposition volume changes will be. The measured deposition volumes are relatively stable for initial liquid level of 1.2mL and 1.0mL. The reason why the 1.0mL line indicates a greater average deposition volume than the 1.2mL is because of the difference in duration of actuation.

Optimal Conditions

Several observations were made from Figure 4. A higher initial fluid level tends to result in higher deposition volume. The exception to this trend was when the initial fluid level was 1.0mL. The average deposition volume was lower for the test conducted with 1.2mL initial fluid level compared with 1.0mL. The cause of this is likely due to the difference in actuation times. A faster actuation time of 4ms compensates for the higher pressure which results from a higher fluid level. Furthermore, the slopes of the curve for higher initial fluid levels are steeper than those with lower initial fluid levels. This is expected since a higher change in pressure from the spring system results from more fluid being dispensed. As more fluid is dispensed, the lower the syringe plunger moves hence reducing the extension of the spring. Also, the deposition volume drops over consecutive measurements caused by air entering the system and obstructing fluid flow. With a faster duration of actuation, there was less air entering the system.

The resolution of the print head system has improved from 88.2nL to 19.0nL assuming the initial fluid level is 1.2mL with an actuation time of 4ms. For higher initial fluid levels, compensation in the software is required for large number of actuations, in order to keep the actuation working properly and to improve consistency.
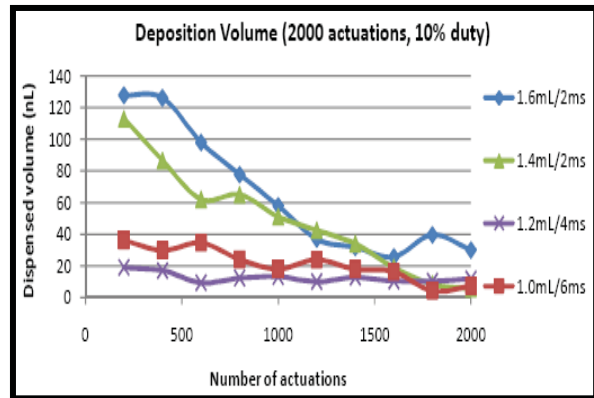

Figure 4. Experimental results

7.   Conclusion

A new actuation system based on a compressed spring was designed for the print-head with a 45% reduction in weight. The resolution of the improved print-head system was measured to be around 20nL. The controlling algorithm was modified to provide more accurate timing and incorporates an automatic mode.

Acknowledgements

Reference

[1]   Paul, K.E., Wong, W.S., Ready, S. and Street, R.A. (2002) *Additive Jet Printing of Polymer Thin-film Transistors.* Palo Alto Research Centre.

[2]   Torsi, L. (2005) OTFT as Plastic Analytical Sensors. Thesis, University of Texas at Austin.

Low Cost Autonomous Guided Vehicle With Obstacle Avoidance Using A Laser Range Finder

D.R. Smith, M. Kubo
The University of Auckland,
Department of Mechanical Engineering,
Mechatronics Engineering,
New Zealand

Abstract:
The project's objectives were to integrate a Laser Range Finder (LRF) into a Field-Programmable Gate Array (FPGA) controlled Autonomous Guided Vehicle (AGV). The hardware and software requirement in implementing the LRF will aid the AGV in achieving its main objective. The AGV's main objective is to successfully avoid and evade oncoming obstacles, on-the-fly, at near to the AGV's maximal velocity, as it navigates environments autonomously. The LRF portrayed a far more accurate and faster representation of the AGV's surroundings as opposed to the ultrasonic sensor that was previously utilized in the AGV. The sensors and actuators were implemented and controlled on a DE2 evaluation board by Altera. This board utilized a Cyclone II Field-Programmable Gate Array (FPGA) for its logic elements and processing requirements. Appropriate algorithms to meet the objectives were implemented into the FPGA using Altera's Quartus II and NIOS II software. The LRF combined with improved algorithms gave the AGV the ability to successfully avoid obstacles on-the-fly and at near to the AGV's maximal velocity.

1. Introduction

An Autonomous Guided Vehicle (AGV) is a mobile mechanical/electrical intelligent system that makes heading decisions based on the surroundings presented to it. For the AGV to detect the surroundings and make correct decisions, appropriate sensors must be in place, many sensors have been utilized on AGV's throughout their history. Some of these sensors include ultrasonic sensors, magnetic guidance sensors, and Laser Range Finders (LRF). AGVs today are competent robots that aid human endeavour throughout many industries such as health and logistics. They significantly reduce labour costs and lead times and can work to their full potential without having to rest; this is an attractive attribute for any organization.

This project was initially started in 2005 by S.Q. NG and J. Chang, utilizing a PC laptop to carry out the AGV's system functions. The project then went through many stages of evolution, in 2006, a Field-Programmable Gate Array (FPGA) was used to replace the PC laptop which gave the project an embedded low cost vibe. In 2007 the Global Positioning System (GPS) and the Obstacle Avoidance System (OASYS) was separated into two independent projects. This was done so each aspect, the GPS AGV and the OASYS AGV could have more resources focused towards each of them.

In 2008 the project was named 'Low Cost Autonomous Guided Vehicle with Obstacle Avoidance using an Ultrasonic Sensor,' by A. P. Tjahyono and J. Pau [1, 2]. That year an ultrasonic sensor was implemented to a stepper motor so 'on-the-fly' sensing could be performed. Also the Vector Polar Histogram Plus (VPH+) algorithm [3] was implemented in the intensions of giving the AGV greater intelligence when dealing with approaching obstacles. The VPH+ algorithm was designed for AGVs that utilized Laser Range Finders (LRF), due to the 2008 project utilizing an ultrasonic sensor the AGV was heavily handicapped. Because of that main constraint, the aim of the current project was to replace the ultrasonic sensor with a LRF and to modify and develop further the software that was implemented in 2008 on Altera's Development and Education 2 (DE2) board. Power consumption was a primary problem with past projects implementation, the 2009 project was to reduce the power consumption significantly so that the AGV can perform for longer durations. Also to integrate an Inertial Measurement Unit (IMU) so position tracking can be carried out effectively. This manuscript will only focus on detailing the implementation of the LRF and the modification of the VPH+ algorithm for, and to better suit an FPGA control system.

2. 2008 Ultrasonic Range Sensing

In the 2008 project by A. P. Tjahyono and J. Pau, the ultrasonic sensor was integrated into the AGV and fixed to a stepper motor to incrementally scan the environment. Due to the way that the ultrasonic sensor was mounted on the AGV resulted in the scan area being restricted to 120° with five sectors, 30° apart. Ultrasonic sensors have many unattractive attributes, some include slow response times, sound absorbing materials cannot be seen, and also the

orientation of the object can hinder the performance of the sensor. The ultrasonic sensor relies on the sound wave that it initially releases into its oncoming environment to be reflected directly back off an object so appropriate calculations can be carried out and ranges can be found. If that initial sound wave is reflected back at an orientation away from the sensor, then the range cannot be found. Due to this fact, if an object that the AGV is trying to avoid is at an invisible orientation, ultimate failure may occur resulting in collision. This is what A. P. Tjahyono and J. Pau found when testing the AGV (as shown in Figure 1).
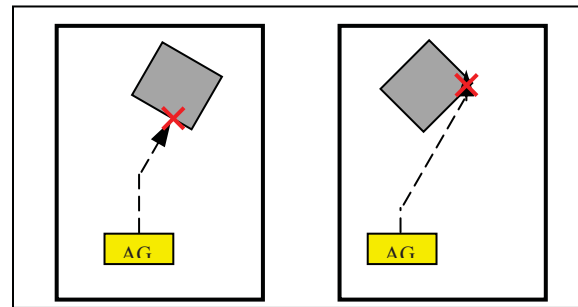

Figure 1: Object orientation creating collision with the AGV during a test run (Reproduced from [1])

3. Laser Range Finder Basics

Laser Range Finders have been predominantly used in the military for judging distances so infantry, snipers, artillery and mechanical infantry can obtain more accurate interpretations of their environments. LRFs today are becoming more and more popular for AGVs due to their many attractive qualities. There are currently two types of LRF sensing methods, the first being the 'time-of-flight' method, this method releases a light beam, then starts a timer and then waits until an object reflects the light beam back. The timer is then stopped and the distance can be calculated, due to knowing the speed of light. The next method is called the multiple frequency phase-shift interferometry method, when the light beam reflects off an

object a frequency phase-shift occurs, knowing this and other light attributes a simultaneous equation can be created and the range of the object can be determined [4].

Today one of the lead manufactures of robotic LRFs is a Japan company named Hokuyo [5]. They manufacture many different types of LRFs varying in price and specifications. There are many attributes that make LRFs an attractive sensor to an AGV, some of these attributes are:

- Very fast response times
- Very fast sampling times
- High resolution
- Large detection ranges
- Can be consistently accurate on most surface colours except on a reflective surface
- Immune to object orientation
- Excellent noise immunity

4. Control System Overview

The control system that was integrated into the AGV was the DE2 board which contained the Cyclone 2 FPGA. The software that was used to program the hardware-software aspect of the FPGA system was Altera's Quartus II. The Quartus II program has a processor builder wizard feature integrated into it. This wizard is called the 'System On a Programmable Chip (SOPC) builder'. The SOPC builder was used to construct the NIOS II processor of the AGV system. Altera's NIOS II software was then used to implement the imbedded C programming language aspect of the system. The system would take in a human controlled input which was a push button on the DE2 board. Pressing specific buttons activated an interrupt request (IRQ) within the NIOS II processor which would either make the system start, stop or pause. Once a human control input resonated throughout the system, the implemented Quartus II system would activate and carry out the

behavioural language that was initially implemented by the user. The Quartus II components and the NIOS II processor would work in unison together carrying out implemented algorithms, storing calculated variables in memory and communicating to the appropriate sensors and actuators. An analogy of this is represented in Figure 2.
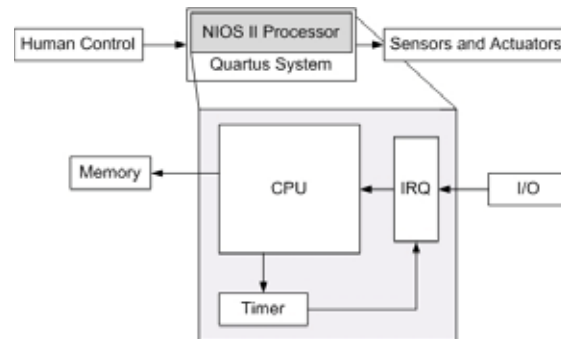

Figure 2: A diagram analogy of the AGV's controls

5. The NIOS II System

A NIOS II system is a customizable processor within Altera's FPGA chips. Design and implementation is carried out through Altera's SOPC builder within the Quartus II program. Once the NIOS II processor peripherals have been assigned, it can then be built 'softly' onto the FPGA. After the processor has been built, NIOS II programming can be carried out. The programming language within the NIOS II processor can either be implemented in embedded C or C++.

6. Laser Range Finder Quartus II Components

The Quartus II components that interacted with the LRF were straight forward. The LRF utilized the RS-232 UART port; therefore the only components that had to be added were in the form of pin declarations and components within the SOPC builder. These pins were directly wired to the NIOS II processor and no Quartus II components other than the pin declarations were needed.

7. Field Programmable Gate Array (FPGA) Overview

The processing system incorporated in the AGV as already specified was the DE2 board manufactured by Altera. The DE2 board included a Cyclone II FPGA along with other useful prototyping features such as multiple I/O configurations and ports, external memories, displays and switches. The DE2 board only had one RS-232 UART port which would become a problem due to many sensors utilizing this port. Due to the ease of prototyping and its processing capabilities the DE2 board was the preferred choice for FPGA system integration.

8. Laser Range Finder Hardware Implementation

As specified earlier the ultrasonic sensor was replaced with a LRF. The LRF that was used was Hokuyo's UBG-04LX-F01. The UBG-04LX-F01 had both USB and RS-232 communication protocols (USB having dominance over RS-232 if both protocols were used at the same time). For the DE2 board to use the USB configuration, appropriate drivers were needed within the FPGA. To save time, the USB of the UBG-04LX-F01 would not be utilized, but instead the RS-232 port was chosen to be used for its communication protocol.

9. Laser Range Finder (LRF) Signal Processing Discussion and Results

To successfully implement the LRF into the DE2 board, communication aspects of the LRF had to be understood. The Hokuyo UBG-04LX-F01 could communicate via either RS-232 or USB, if both communication protocols were utilized simultaneously; the USB would have dominance over the RS-232 communication.

Figure 3: A data request from host pc to the Laser Range Finder (LRF) (Reproduced from [6])

The LRF's communications are based on Hokuyo's SCIP 2.0 protocol [6]. Reviewing Hokuyo's Communication Protocol Specifications SCIP 2.0, it was found that the LRF was very versatile in the way it obtained, processed and communicated its data. The transmitted and received data to and from the LRF was in the form of ASCII characters. First to carry out a reading, a data request code had to be sent to the LRF, the data request code was specific, detailing the type of distance data that was desired to be transmitted back to the host (as shown is Figure 3). The data request code is made up of either twelve or fifteen ASCII characters, depending on the mode of operation which is requested.
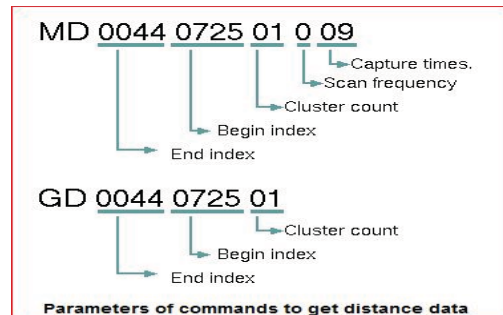

Figure 4: The data request code definition based on the SCIP 2.0 protocols (Reproduced from [6])

The modes of data transmission are specified in the first two ASCII characters of the data request code. The first character can either be an 'M' or a 'G' (the data request code is case sensitive). 'M' signifies the nth amount of scan times (aka capture times, as

shown in Figure 4) that the LRF will transmit back to the host before it stops transmitting data. As seen in Figure 5, 'G' signifies that the LRF will only transmit one scan of the environment before it stops transmitting data. The second ASCII character in the data request code can either be a 'D' or an 'S'. 'D' signifies the distance data obtained will be represented using three ASCII characters. This output type gives a distance resolution of 1 millimetre. 'S' signifies the distance data obtained will be represented using two ASCII characters. This output type gives a distance resolution of 65 millimetres, which is less resource consuming than 'D' and is the most appropriate when integrating a LRF into an FPGA.
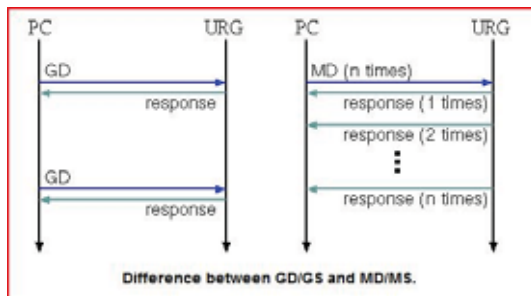
Figure 5: The difference between the 'G' and 'M' transmission mode (Reproduced from [6])

The next four ASCII characters signify where on the 360° scan the LRF stops capturing the distance data, this is in the form of integers. As seen on Figure 8, these four ASCII characters are '0044' (end index). Knowing the incremental resolution of the LRF is 0.36°, the angle at which that code represents can be found. For example, the end index multiplied by the resolution, which in Figure 6's case is equal to 15.84° from the reference point. The next four characters after the end index is the start index, these are in the same form as the end index. As seen on Figure 4, these four ASCII characters are '0725' (start index), using the same method as above to work out

the angle, it was found the LRF started capturing the distance data at 261° from the reference point. Using both the end and start index's in Figure 4, the distance scan range is found to be between 261°, and 15.84°, which produced a scan range of 245.16° (as shown in Figure 6).
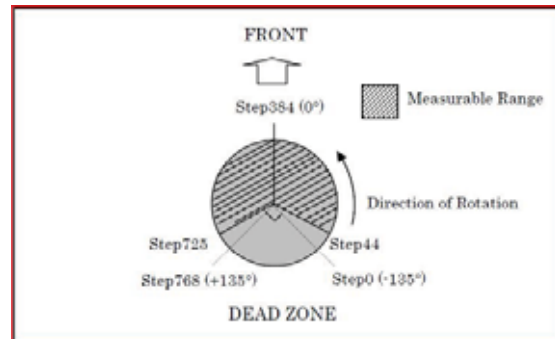

Figure 6: The end and start index reference points (Reproduced from [6])

The next two ASCII characters signify the cluster count (as shown in Figure 4), these characters have to be in the form of an integer. The cluster count is simply a merging function. For example a cluster count of '03,' represents for every three distance data readings received will be merged together into one distance data reading.

The next one ASCII character signifies the scan frequency (as shown in Figure 4). This is in the form of an integer. This is only used in continuous scan capturing; if the scan frequency was '2' then every second scan would be ignored.

The last two ASCII characters signify the capture times (as shown in Figure 4). This is also in the form of an integer. This is also only used in continuous scan capturing, as specified earlier, this is the amount of scans the LRF carries out.

Figure 7: The outputted data of the UBG-04LX-F01 in HyperTerminal

Initially to verify that the LRF's communications were valid, the LRF was connected to a host PC and Hyper Terminal was utilized to send and receive serial data to and from the LRF. As seen in Figure 7, when a data request had been sent from the host to the LRF the following would occur:

1. The LRF would then echo the data request back to the host (MD0044072501007)
2. Output a checksum value (99b)
3. Output a time stamp encoded in SCIP 2.0 format (4PlgG)
4. Then output the following distance data initially specified by the data request.

The distance data was outputted as 64 ASCII characters, plus a single ASCII character checksum, followed by a return ASCII character to start a new line. The ASCII characters were encoded in the form SCIP 2.0 protocol. Two return line ASCII characters were outputted by the LRF to signify that it had finished carrying out the instructions set forth by the data request code.

For the DE2 board to communicate to the LRF, communication protocols had to be determined. The LRF had both a USB and RS-232 outputs and the DE2 board had the appropriate hardware to accommodate both of the protocols. The RS-232 communication protocol was used because the USB host on the DE2 board needed appropriate drivers for the LRF and would be too time consuming to implement. Considering the RS-232 UART communication protocol had already been set up by the 2008 team for the GPS, it was easy enough to adjust focus to the LRF.

10. Hokuyo's SCIP 2.0 Decoding Protocol

The efficiency of the NIOS II code produced on the DE2 board was crucial due to limited resources within the FPGA chip. To implement the appropriate code for the LRF many hurdles were faced and overcome. One major problem that was solved was the baud rate of the LRF and the DE2 board; initially they were not synchronous with one another, even though both the baud rates visually matched. Initially this made it very difficult to obtain any data from the LRF due to synchronous errors. To overcome this problem a back and forth solution was found by setting the baud rate slower on both the LRF and the DE2 board and only obtaining one distance data scan per every data request. This minimized the amount of data transferred and reset the synchronisation after every request resulting in eliminating all synchronous errors.

Once the data was received from the LRF it was sorted into an array and decoded in a function using the SCIP 2.0 protocol, an example of decoding 2-characters is as follows:

1. Receive a segment from a scan (C, B) ANSCII = (43H, 42H) Hex
2. Add (30H) Hex to above
3. Equals (13H, 12H) Hex = (010011, 010010) Binary
4. Combine the two (010011010010) Binary
5. Equals (1234) decimal = 1234mm

It was found that there were many checksum errors that occurred during every scan of the laser. There are many reasons for these errors, but the main reason is usual due to the surface type in which the LRF is obtaining distance from. Raw data obtained from the LRF via the DE2 board is shown in Figure 8, as seen, there are many outliers

and zeros. These outliers and zeros if left like this will cause major problems when the AGV is estimating its next move; therefore they had to be eliminated.
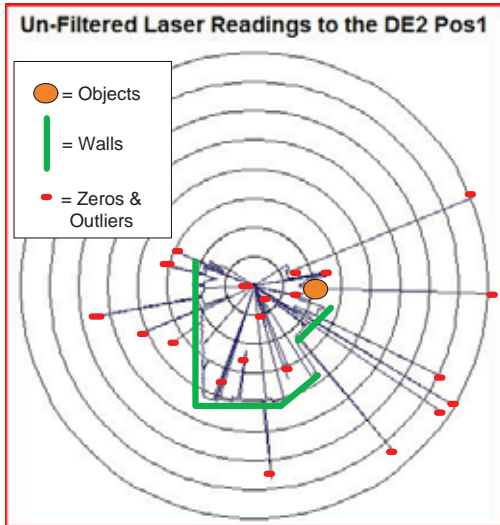

Figure 8: A 240° scan obtaining distance data from the LRF, many zeros and outliers

An 'extreme outlier filter' algorithm was implemented into the NIOS II code to remove all of the outliers. Knowing the three previous already obtained distance data, and also knowing that the outliers produced did not occur in groups (singular), the 'extreme outlier filter' algorithm could be easily implemented. As seen in Figure 9, an outlier is going to produce two large lengths in relation with the present and the past distance data. If length one AND length two are both above a threshold value, then an outlier is present, it is then replaced with the present non-outlier distance data. As seen in Figure 10, the 'extreme outlier filter' was successful and it also minimized the error zeros that were produced.
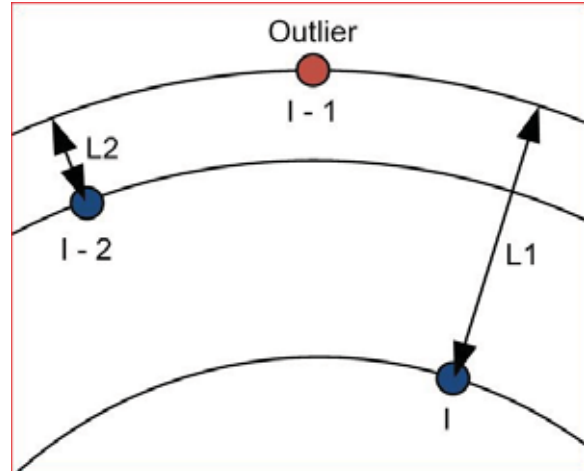
Figure 9: The visual representation of the characteristics of an outlier
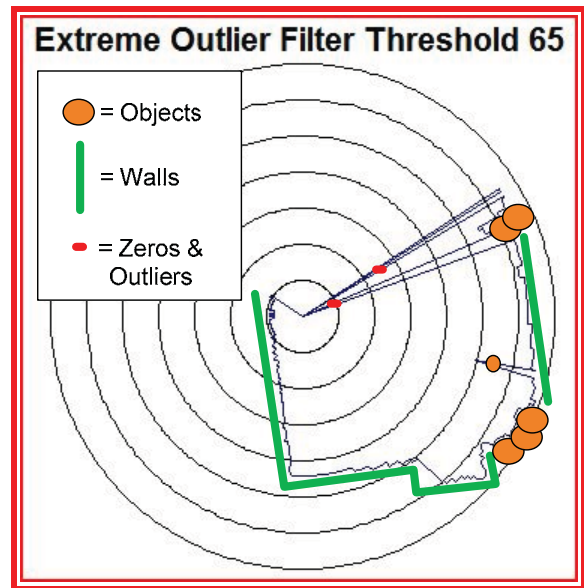
Figure 10: Distance readings from the LRF with the extreme outlier filter

Next was to remove the error zeros, an algorithm was easily implemented by ignoring zeros and replacing it with the previous valid distance data. Figure 11 shows the zero filter eliminating the zeros and creating accurate distance readings from the environment presented to it.
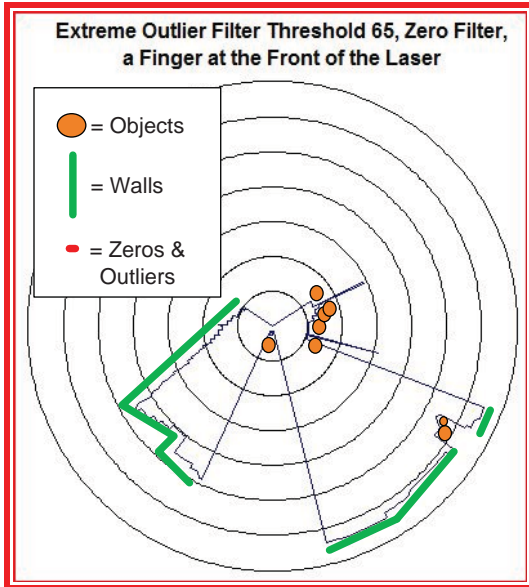
Figure 11: Distance readings from the LRF with the extreme outlier and zero filters

The overall accuracy of the LRF was tested using a tape measure and objects placed at certain distances in front of the LRF. The LRF took three scans of the environment each with different object configurations. It was found that the LRF produced accurate and repeatable representations of the environment with an error of plus or minus its linear resolution, which was 65 millimetres. This error is easily seen as steps or saw teeth in the above radar plots (shown in Figure 8, 10 and 11). The 65 millimetre error produced by the LRF could affect the AGV in confined areas, but in open large areas the errors would be insignificant.

11.   Obstacle Avoidance and Path Tracking Techniques

The 2008 obstacle avoidance techniques implemented in the NIOS II code was used as the foundation for the improvement of the 2009 system. As already specified, the 2008 project utilized the VPH+ obstacle avoidance techniques [1]. There were many improvements and refinements made to the 2008 obstacle avoidance techniques. This was due to having a much more powerful

distance tracking component (the LRF). Figure 12 shows a flow chart representing the algorithms that were carried out to find the best sector to travel.
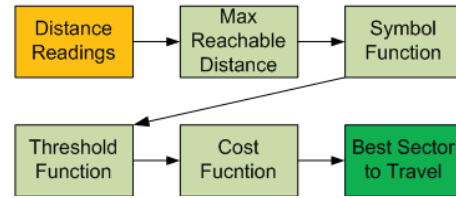

Figure 12: The processes carried out to find the best sector to travel

12.   Truncation Discussion and Results

The 2008 system obtained five distance readings at 30° angle intervals (shown in Figure 13). The scanning range was restricted to 120°. To gain a better representation of the AGV's surroundings so greater obstacle avoidance could be carried out, stressed the requirement for more sectors. The LRF eliminated the flaws of the ultrasonic sensor and also allowed for more sectors to be scanned, along with a larger scanning range of 180°. It was decided that 25 sectors were going to be implemented in this system. This was partly due to being divisible by the output readings from one LRF scan (525 distance readings for the 180°). Also 25 sectors were sufficient enough to produce an accurate representation of its environment. To convert the 525 raw LRF sectors into an equivalent 25 sector representations, a truncate function was implemented. The truncate function was represented by the equation:

$$D_i = \min\{d_{21 \times i + j}\} \quad (1)$$
$$j = 0,1,2,...,21$$
$$i < 25$$

In Equation (1), D_i represents the new truncated distance readings for each of the 25 sectors, d represents the raw 525 sector distances obtained by one LRF reading. As shown in Equation (1), the minimum

distance has dominance over any other distance. This is so that the AGV knows in the truncated 25 sectors there is a small distance value, which relates to an obstacle and will be avoided if small enough. Figures 14 and 15 represent a truncation occurring, the radars show 525 sectors being successfully truncated down into 25 sectors.
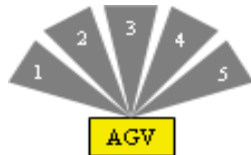

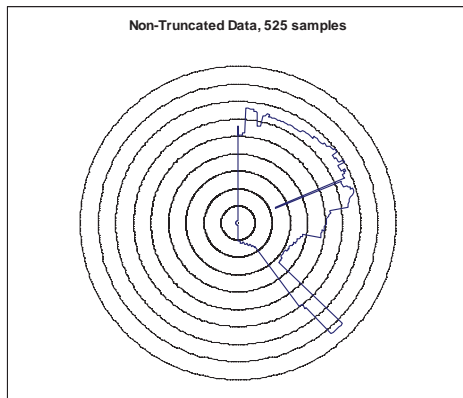**Figure 13: The 2008 AGV examining five sectors (reproduced from [1])**
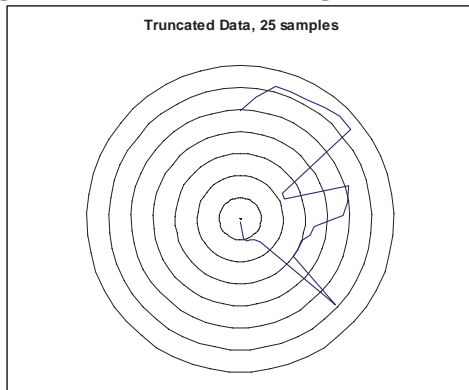

Figure 14: 525 distance readings from the LRF

Figure 15: The results of a truncation of the 525 distances into the equivalent 25

13. Cheap Max Reachable Distance Discussion and Results

A major problem arose when the 25 sectors were implemented into the system. The original max reachable distance function was very resource consuming. The purpose of the original max reachable distance function was simply to take in the 25 sector distance readings and modify it to take into account the AGV's radius. More simply it creates a uniform inner shell of the original distance data, with a width of the AGV's radius (shown in Figure 16). The original max reachable distance function's execution period was very slow and this was due to using an algorithm that had many nested compare loops and utilized heavy mathematical equations. The period of execution of the function was of an exponential factor of how many sectors had to be modified. Therefore modifying the system from five sectors to 25 sectors and executing the original max reachable distance function resulted in large processing times of approximately 120 s/scan. This time period would not be feasible when carrying out successful obstacle avoidance therefore it had to be modified to better suit the resource constraints of an FPGA system (using a PC, the processing times would be faster due to having dedicated resources).

The solution to the resource consuming problem was the creation of a cheap max reachable distance function that had a quick execution time. This function was an imitation of the original max reachable distance function and produced similar results, but the method in which it modified the distance readings was very different. The cheap max reachable distance function's process comprised of four main steps:

1. Take in the 25 distance reading of each sector.
2. Subtract each of the 25 distance readings by the radius of the AGV. This is shown in Figure 16, it is also shown that the AGV could collide with the wall, therefore an extrusion of a protrusion function was needed, and this was the next step.

3. To extrude a protrusion in the environment a protrusion first had to be identified. As seen in Figure 16, it is clear when a protrusion has occurred. This can be identified as either a step up or step down in the distance reading value. Once a step up or step down characteristic has been identified the current distance reading will be carried over to the previous distance reading, this is a simple way of extruding a protrusion, and this is also shown in Figure 17.

4. Lastly output the modified max reachable distance data for appropriate sector weighting.
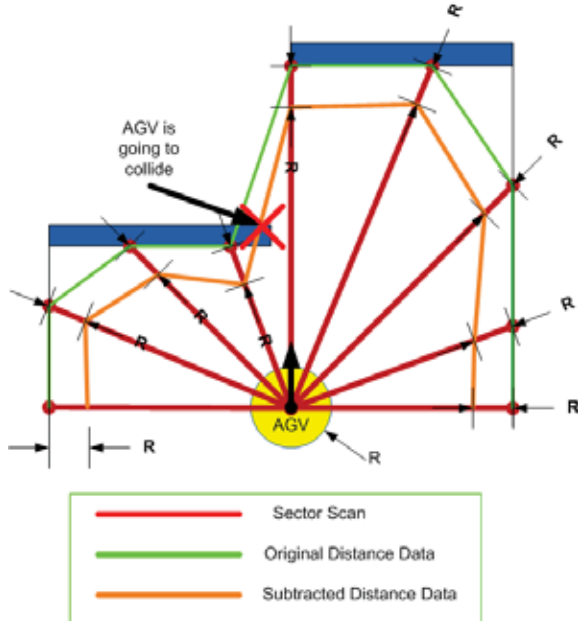
Figure 16: The results of a radius subtraction on the original distance data
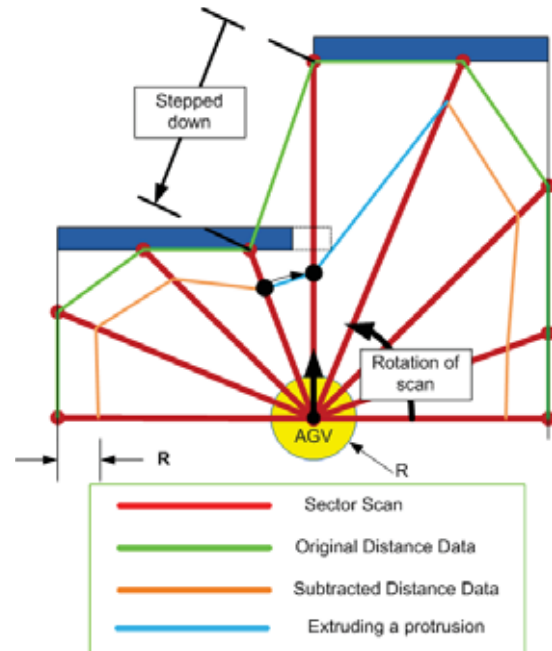
Figure 17: The extrusion of a protrusion of the subtracted distance data

The results of operation of the cheap max reachable distance function were satisfying. The processing time of carrying out the function was immediate and the output was very similar to the original function. A comparison of the original verses the cheap function is shown in Figure 18.
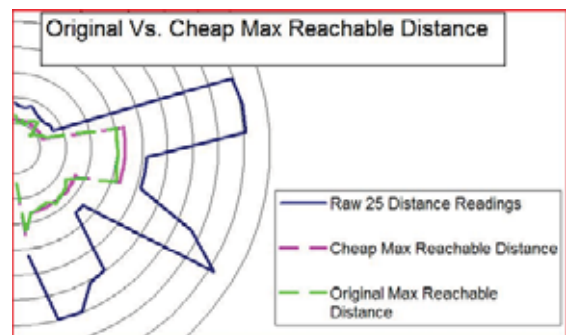

Figure 18: The radar scan results of cheap max reachable distance vs. max reachable distance functions

14.   Testing Results and Discussion

A number of environments were created to test the overall effectiveness of the AGV's systems. Obstacles were strategically or

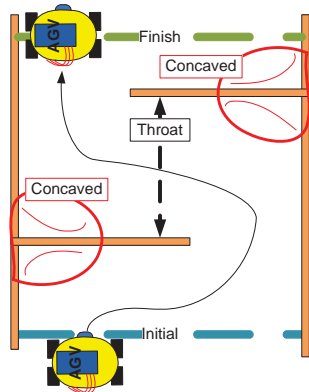randomly placed in and at specific orientations within these environments.

Figure 19: The AGV navigating a tight 'S' bend

The first experiment carried out was a simple 'S' bend, this is shown in Figure 19. This experiment was where most of the AGV's testing was carried out. The 'S' bend was created to have specific attributes to test particular areas within the AGV's systems. These attributes were:

- The initial position being directly in front of a wall. This tested the AGV's start up reaction times and overall reaction times.
- The throat of the 'S' bend was the minimum distance the AGV could pass through. This tested to perceive if the environment that was being created within the AGV from the feedback from the outside environment was of an accurate portrayal.
- The 'S' bend had concaved areas. This tested to distinguish if the VPH+ cost function was functioning accurately.
- The 'S' bend had two protruding walls. This tested the cheap max reachable distance function.

In the initial stages of improving the system, the AGV could not navigate through the 'S' bend. In the maturing stages, the AGV slowly improved navigating the 'S' bend, due to such improvements like the cheap

max reachable distance and the IMU being integrated into the system. The final AGV system could navigate the 'S' bend with ease, from any initial starting position and also could execute the 'S' bend at close to its max velocity.
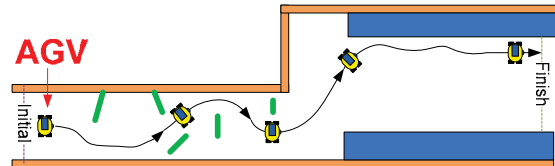

Figure 20: The AGV navigating a hallway with obstacles

The second experiment subjected to the AGV was within a long hallway. The hallway initially had a skinny width which funnelled outwards into a larger width, as shown in Figure 20. Obstacles were scattered randomly throughout the skinny section of the hallway. It was made sure that the AGV could pass by the obstacles. The aim of this experiment was to test if the AGV could navigate small confined spaces for long durations, then be suddenly subjected to large open areas. Also another aim was to confuse the AGV over a long distance, and immerse the AGV in an environment that man readily navigates. This experiment was carried out a number of times. It was found that the AGV had trouble avoiding objects that were of a reflective nature. This problem was obvious due to using a LRF to track obstacles. Obviously the colours of the obstacles were going to be a function of how well the AGV avoids them. The reflective obstacles were replaced with ideally coloured obstacles. The AGV then could navigate the long hallway successfully and with ease at one hundred percent repeatability and at close to its full velocity.
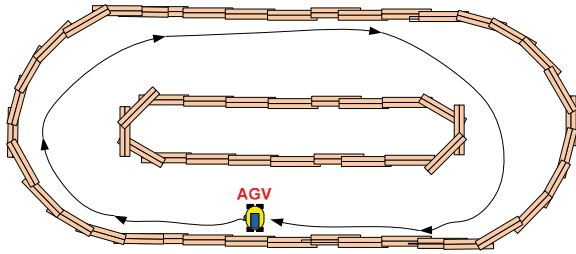
Figure 21: The AGV navigating an oval track

An oval track was set up for the third and final experiment, as shown in Figure 21. The aim of the oval track was to examine if the AGV could continuously navigate a completely closed off area without error. The results of the experiment were very pleasing, the AGV carried out four laps of the oval track flawlessly and at close to peak velocity for the whole duration of the experiment.

15. Conclusions

- The LRF was successfully incorporated into the AGV. This gave the AGV a very accurate representation of the environment and the obstacles within the environment. This was all implemented through new specialised circuitry, Quartus II components, and embedded C algorithms.
- A truncation algorithm was successfully implemented into the AGV so 25 sectors could be analysed through the VPH+ algorithm.
- The VPH+ algorithm was successfully modified to better suit an FPGA processor. This was so data could be processed much more efficiently, and was achieved through the implementation of the cheap max reachable distance algorithm.
- Reflective surfaces attracted the AGV when carrying out the obstacle avoidance process.
- The AGV's overall obstacle avoidance was adequate and was very promising in a number of different environments, as

long as there was an absence of obstacles with reflective surfaces.

References

[1] A. P. Tjahyono. (2008). *Low Cost Autonomous Guided Vehicle with Obstacle Avoidance using an Ultrasonic Sensor*. 4th Year Project MT-40, Department of Mechanical Engineering, The University of Auckland.

[2] J. Pau. (2008). *Low Cost Autonomous Guided Vehicle with Obstacle Avoidance using an Ultrasonic Sensor*. 4th Year Project MT-32, Department of Mechanical Engineering, The University of Auckland.

[3] Gong, J., Duan, Y., Man, Y., & Xiong, G. (2007). *VPH+: An Enhanced Vector Polar Histogram Method for Mobile Robot Obstacle Avoidance*. IEEE Conference on Mechatronics and Automation (Harbin), 2784-2788.

[4] Optics Arizona. Phase Shifting Interferometry. Retrieved June 21, 2009, from **http://www.optics.arizona.edu/jcwyant/Optics505(2000)/ChapterNotes/Chapter09/phaseshiftinginterferometry.pdf**

[5] Hokuyo. Optical Data Transmission Devices. Retrieved June 21, 2009, from **http://www.hokuyo-aut.jp/**

[6] Hokuyo. URG Programming Guide. Retrieved June 21, 2009, from **http://www.hokuyo-aut.jp/cgi-bin/urg_programs_en/index.html**

Design, System Identification and PID Control of an Ionic Polymer Metal Composite Actuated Rotary Mechanism

David Liu

The University of Auckland,

Department of Mechanical Engineering,

Mechatronics Engineering,

New Zealand

Abstract:

Ionic Polymer Metal Composites (IPMC) is a novel material with unique electrochemical mechanical properties which allow it to be used as both a smart actuator and sensor. This paper describes the work that was carried out to verify if IPMC transducers can be used to actuate a rotary mechanism. An experimental testing apparatus was used to measure the free bending mechanical properties of the IPMC cantilever strips. Data from these preliminary tests was used to design the rotary mechanism. Open loop characterization of the fully assembled mechanism was then conducted to develop an empirical model of the system. A Proportional, Integral (PI) controller was developed using simulations and tested on the rotary mechanism to control the position of the rotary mechanism. Dead-zone compensation was added to improve the steady state response. Experimental results show that the classical controller is successful in actuating the rotary mechanism to microscopic deflections.

Keywords: *Ionic Polymer Metal Composite (IPMC), System Identification, PID, Control.*

1. Introduction

IPMCs are a category of electro-active polymer that has been subject of considerable interest over recent decades for their potential to be used as novel transducers. The smart material is composed of a flexible ionomeric membrane sandwiched between 2 thin electrode layers made from gold, silver or platinum [1]. The ionic polymer possesses the unique ability to convert electrical energy applied across its thickness to mechanical energy and vice versa. When a voltage is applied across the thickness of the IPMC, an electric field is created across the electrodes. Mobile cations become attracted to water molecules and migrate towards the cathode boundary layer of the material while the anions remain stationery [1][2][3]. This process occurs within milliseconds. The accumulation of water molecules in the cathode side of the cantilever strip causes the material to mechanically deform by bending and contracting towards the anion side. This concept is shown in Figure 1. The presence of water is critical to the functionality of the novel material [4]. IPMCs can produce large tip deflections but small tip force outputs from low voltage signals when fabricated in a cantilever configuration. This special trait combined with other advantageous properties such as being flexible, low weight and biocompatible

make it ideally suited for use in various engineering applications that can not be actuated by commercially available active materials or traditional actuators currently in the market. Many studies have been carried out to investigate the free bending behaviour of IPMC actuators [5]. However, there has been insufficient research to determine if they can reliably actuate engineering mechanisms such as a rotary linkage. Therefore the primary objective of this research is to investigate if these smart actuators are capable of actuating and controlling the position of a rotary mechanism.
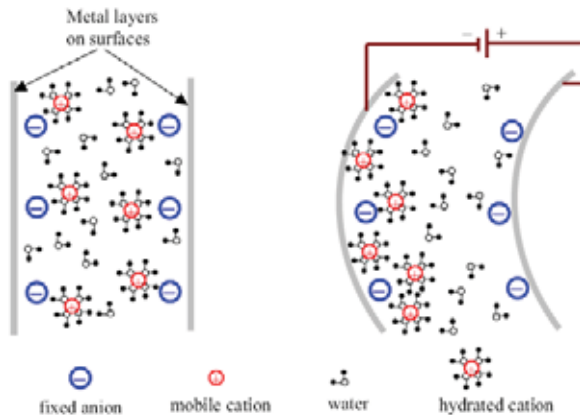

Figure 1: Diagram showing the migration of hydrated cations across the IPMC membrane. Reproduced from [6].

2. Specifications of IPMC Actuators

The IPMC cantilever strips used in this research were acquired from Environmental Robots, Inc. (ERI) in Albuquerque, USA. They are Nafion® 117 class ionic polymers and contain Lithium (Li+) ions. This polymer membrane was sandwiched between electrodes made from gold. The IPMC strips have a thickness of approximately 0.6mm, a length of 30mm and a width of 10mm. These custom strips are thicker than conventional IPMC actuators to increase the tip output force properties of the material at the expense of

reduced tip deflections. Throughout the duration of these studies, the IPMC actuators were used only once before being rehydrated for at least 15 minutes. The strips had a unique curvature which varied between experiments due to a combination of its current hydration level, prior use and material degradation.

3. Testing Apparatus

An experimental testing apparatus was used to characterise the free bending behaviour of both the IPMC strips. To hold the strips in place during experiments, a mounting clamp made from aluminium with a plastic interface was used to provide electrical isolation. Electrodes made from copper were fabricated to provide a voltage signal to the IPMCs. A Banner LG10A65PU Laser displacement Sensor was used to measure the tip displacement of the cantilever strips. The laser sensor can capture data with an analogue resolution of less than 10 μm at a distance of 100 mm. To measure the blocking force of the actuators, a SS-2 Precision Force Sensor from Sherborne Sensors Limited was used. The sensor produces an analogue output and was calibrated to measure +/- 30gf with a sensitivity of 6.0 mV/V. An interfacing PCB circuit was designed to provide power to the testing apparatus and direct the flow of sensor readings. A National Instruments PCI-MIO-16XE50 Data Acquisition (DAQ) card was used to perform data acquisition tasks and was also used to transmit control signals from a LabVIEW software program to the test rig. The software program provides an interface between the computer and testing apparatus and the user. It also records data readings for later analysis. The schematic diagram of the testing apparatus is shown in Figure 2.
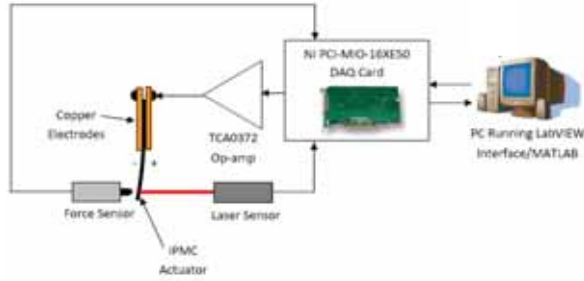
Figure 2: Schematic Diagram illustrating the layout of the sensor and equipment of the experimental apparatus. Reproduced from [7].

3. Free Bending Deflection Results

Step voltages from -4 V to +4V at 1V intervals were applied and the tip deflection behaviour of the IPMC strips (#1 and #2) was recorded over a period of 100 seconds. At least 3 experiments were conducted for each step voltage. The typical response is a rapid initial deflection which tapers off as the actuator reaches peak displacement. Back relaxation then causes the IPMC actuator to slowly bend back towards the initial starting position of the test. Figure 3 shows the average peak displacement response of both IPMC strips. When actuated with a +4V step voltage, an average deflection of 10.27mm is produced for IPMC #1 and 8.959mm for IPMC #2. With a -4V step voltage, the average deflection produced by IPMC #1 is -7.505mm and -7.317mm for IPMC #2.

4. Free Bending Blocking Force Results

The same input step voltages were used to characterise the blocking force output of the IPMC strips. When actuated by the voltage, the tip force of the actuator rapidly increases until peak force is reached and then gradually decreases due to back relaxation. Figure 4 shows the average peak blocking force response of both IPMC strips. IPMC #1 produced an average force output of 5.521gf with a +4V input signal and 5.320gf with a -4V input signal. IPMC #2 also

produced very similar average output forces with 5.265gf with +4V and 5.500gf with -4V.
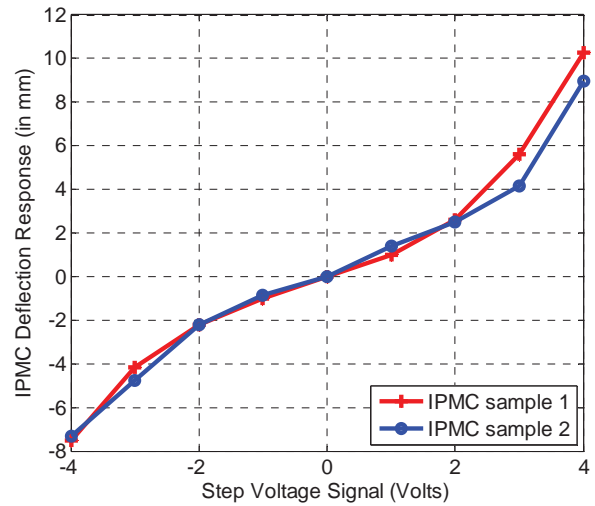

Figure 3: Averaged IPMC peak deflection response for both IPMC strips up to +/- 4 Volts
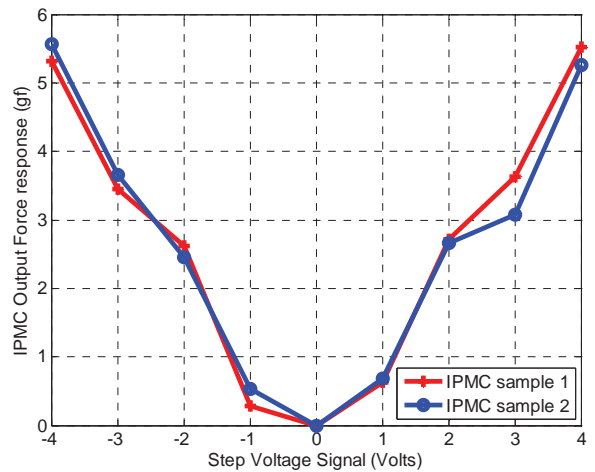

Figure 4: Averaged IPMC peak blocking force response for both IPMC strips up to +/- 4 Volts

5. Design of Rotary Mechanism

The tip displacement and force results from the free bending tests were used to design the rotary mechanism. Aspects of the device such as the weight and friction of the bearings were reduced to minimise the force required to actuate it. The final design was rapid prototyped using stereo lithography

with a precision of up to 100 μm. It is made from using Acrylonitrile Butadiene styrene (ABS) which has a density of 1.19 mg/mm^3. Figure 5 shows the final prototype of the rotary mechanism. The assembled prototype is composed of 3 components. An upper base with a built in bearing was designed to be held in place by the clamps from the testing apparatus. The rotary linkage has a length of 30.1 mm, a width of 20.0 mm wide and total weight of 1.1 g. A component was also designed to hold the stainless steel axle in place during assembly to prevent it from sliding inside the bearing. At the top end of the rotary linkage is a flap tat extends above the device to provide an ideal surface for the laser sensor to get readings from.
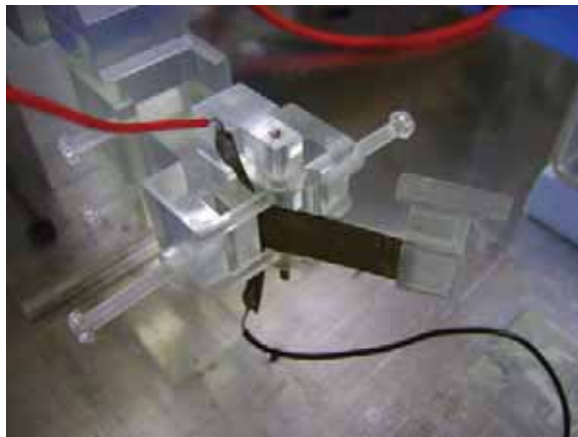

Figure 5: Image of the rotary mechanism prototype with a single IPMC strip and actuated by -4 V.

Experiments determined that the average blocking force of the rotary mechanism is 0.084 gf with a standard deviation of 9.725x10^{-5} gf.

6.   Open Loop Characterisation of Rotary Mechanism

With the rotary mechanism designed, the next step was to characterise the open loop behaviour of the device. Data from these tests would be used to develop an empirical model of the assembled system for controller design. Step voltages from -4 V

to +4V at 1V intervals were applied to the IPMC actuator for 100 seconds and the tip displacement of the rotary mechanism was recorded. The characteristic response is similar to the freed bending tests with a fast initial rise in displacement. Once peak deflection has been reached, the mechanism slowly bends back towards the starting position. IPMC strip #1 was used in these experiments because the actuator produced superior bending and deflection capabilities. The rotary mechanism was submerged in de-ionized water during testing in an effort to create a more repeatable and ideal testing environment. Figure 6 shows the averaged peak deflection results of these experiments.
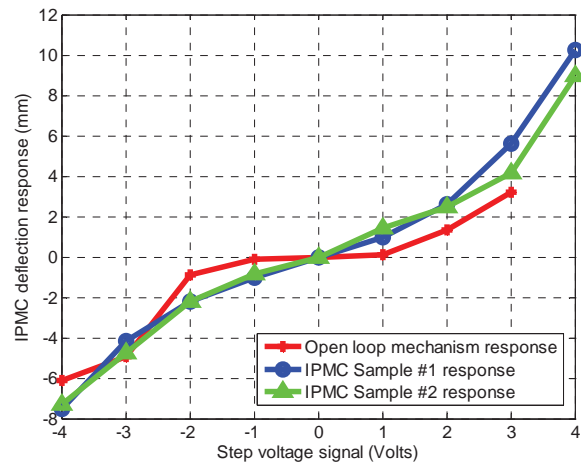

Figure 6: Comparison between the averaged peak deflection response of the rotary mechanism and the free bending behaviour of both IPMC strips with +/- 4 Volts.

When IPMC #1 was actuated with a +3V step voltage, an average peak deflection of 3.227mm was produced while a -3V voltage signal produced an average peak deflection of -4.928mm. The rotary mechanism has a dead-zone between +/-1V indicating that the mechanism cannot be reliably actuated using these electrical potentials. Although there is a clear loss in deflection due to factors such as friction and water resistance, the results show that a single IPMC strip can actuate

the rotary mechanism and produce sizeable deflections.

7.   Development of Empirical Model

The intended application for such a rotary mechanism is eventually for robotics or similar engineering mechanisms and will only be actuated in low frequencies. Under such situations, only the transient and steady state response is of interest. Therefore, a transient response analysis was performed on the open loop step response tests to determine information on the gain, time delay and time constant of the system. An empirical curve fitting method similar to Kanno et al. [8] was used to develop a model of the system. A maximum voltage range of +/-3V was chosen because prior studies have also limited the excitation voltage range to approximately +/- 3 V to prevent rapid dehydration and possibly damaging the IPMC strips [9][10][11]. The deflection response for a -2 V step voltage was used to develop the empirical model. With a dead zone of +/- 1 V, the deflection response of -2 V was selected because it is the central value in the effective voltage actuation range of 1- 3 V. The best data sets were averaged together to minimize the effects of noise and the variability between tests. The Matlab functions FMINSEARCH and BALRED were used to derive a 3rd order transfer function to model the displacement response of the rotary mechanism shown in equation 1.

$$T(s) = \frac{-8.081s^2 + 43.18s + 1.173}{s^3 + 360.3s^2 + 120.1s + 2.765} \quad (1)$$

The transfer function is stable and closely matches the experimental data in both the time and frequency domain. Figure 7 shows a comparison between the averaged experimental and third order empirical

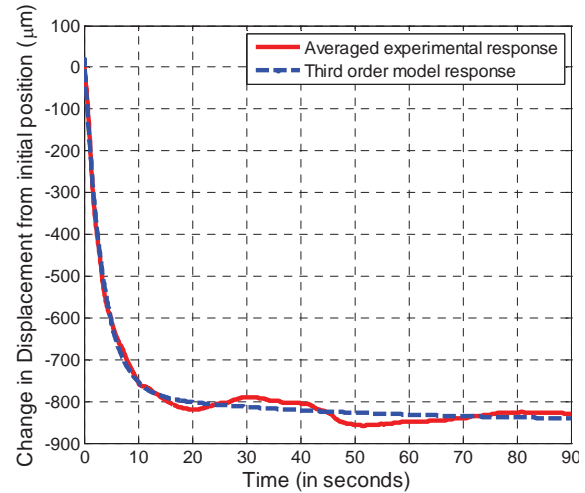model displacement response from a -2V step voltage signal.

Figure 7: Comparison between the averaged experimental and 3rd order empirical model response to a -2V step voltage

8.   Controller Design

A PI controller was designed using pole placement techniques to control the position of the rotary mechanism. Controller gains were tuned with the use of pole-zero maps. The control objectives were to: 1) respond to a step reference signal with minimal overshoot of less than 20%; 2) be able to track the reference position with minimal steady state error; 3) avoid saturating the IPMC actuator with +/-3V control effort for more than a few seconds; and 4) reduce the settling time of the rotary mechanism response to less than 15 seconds. The settling time of the response was considered as within +/- 5% of the steady state position. The control effort is the voltage required to correct the current error in the system and is calculated from the controller. For these control experiments, the rise time of the displacement response was calculated from 10% to 90% of the steady state value. Simulated tests revealed that the inclusion of an integral component eliminated steady state error as anticipated. A derivative component was not used because prior open

loop deflection tests showed that the fully assembled rotary mechanism does not exhibit significant oscillatory behaviour at low frequencies and amplify noise from the laser sensor. It was found that a PI controller produced the best response characteristics when the poles are placed solely on the real axis with no imaginary component. After an extensive testing process, a PI controller was designed with a proportional gain of $k_p = 10$ and an integral gain tuned to be $k_i = 2.1$. When digitalized using the bilinear (Tustin) transformation and a sampling time of 0.1 seconds. The controller is expressed as equation 2.

$$G_p(z) = \left(\frac{10.105z - 9.895}{z - 1} \right) \quad (2)$$

9. Closed Loop Control Testing Method

Three arbitrary reference displacements (300 μm, 500 μm and 700 μm) were chosen for the position control experiments. A slow sampling time of 0.1 seconds (10Hz) was used to run the digital closed loop control

system based on the low bandwidth of the mechanism due to the long rise and settling time responses observed in prior open loop experiments. Figure 8 shows the real time Simulink control system used to test the controller on the actual rotary mechanism.

10. Experimental Results and Discussion

Figure 9 shows the closed loop displacement response of the PI controller to targeted positions of -300, -500 and -700 μm. From inspection of the -300 μm displacement response, the rise time is 4.5 seconds, there is no overshoot present in the response, and the settling time is 7.5 seconds. A response with a rise time of 0.9 seconds, no overshoot and a settling time of approximately 1 second was produced for a targeted position of -500 μm. The -700 μm targeted position has a response with a rise time in the order of 1.7 seconds, an overshoot of 5.829 % and a settling time of approximately 3.3 seconds. The typical voltage control effort response is to initially saturate the IPMC for a maximum of up to 1.7 seconds and then drop the voltage as the rotary mechanism
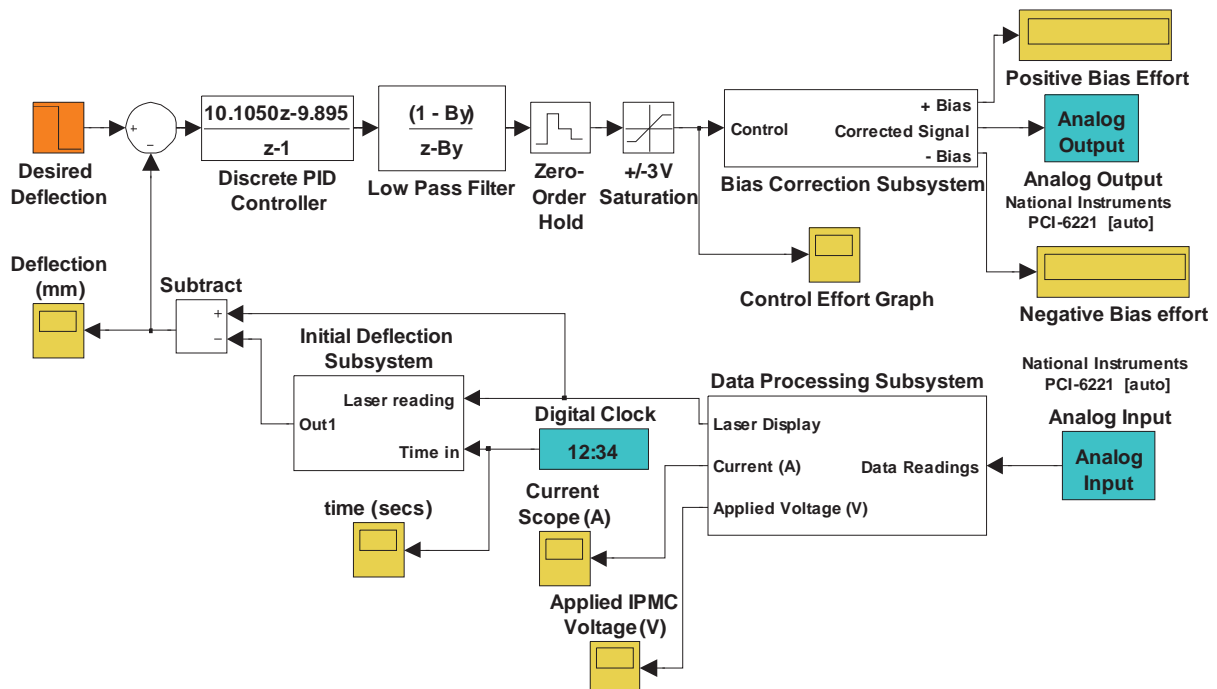
Figure 8: Schematic diagram of the real time closed loop system

reaches steady state. Once at steady state position, the controller gradually increases and oscillates the control voltage to maintain position and reduce the steady state error. However, this causes the rotary mechanism to slowly oscillate in and out of the targeted position and never truly settling. Figure 10 shows the voltage control effort response of the PI controller for a -700 μm targeted displacement.
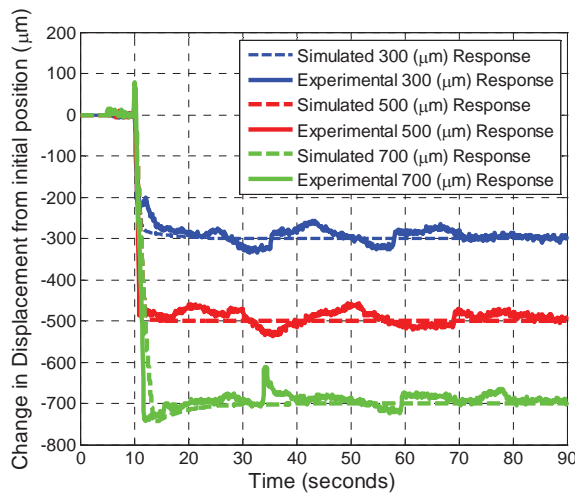

Figure 9: Experimental displacement response of a Pole placement PI Controller for a -300, -500 and -700 μm targeted displacement

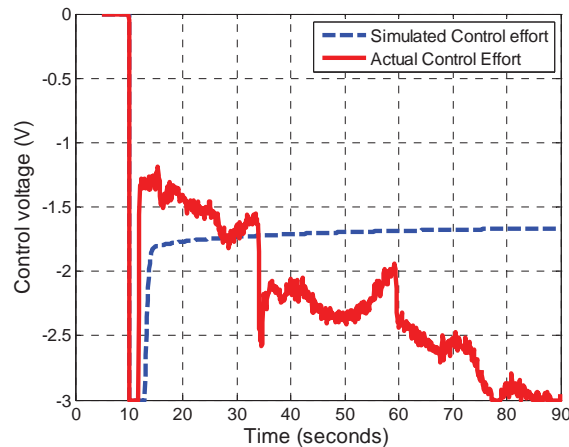**Figure 10:** Voltage control effort of a Pole Placement PI Controller for a -700 μm targeted displacement

A reference position dead-zone of +/-5% was added to reduce the oscillations and the experimental results are shown in Figure 11. The schematic diagram shown in Figure 8 was modified so that when the rotary mechanism was within the +/-5% error band, the integral component of the PI controller would be held constant despite if the rotary mechanism is not exactly at the specified target displacement.
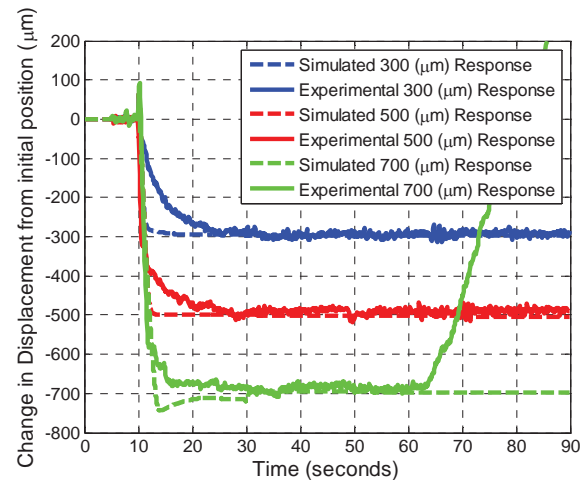

Figure 11: Experimental displacement response of a PI Controller with dead-zone compensation for a -300, -500 and -700 μm targeted displacement

Experimental results show that once the rotary mechanism reached steady state, it was able to stay within the +/-5 % error band. The rise time and overshoot differs from prior tests due to the variability in IPMC behaviour and different clamping conditions between tests. Despite these changes, the modified controller was able to successfully meet all the control objectives. A decline in displacement is noticed in the -700 μm due to the controller saturating before the end of the experiment. Figure 12 shows the voltage control effort response of the PI controller with dead zone compensation for a -700 μm targeted displacement. It can be observed that the gradual increase in control voltage is considerably smoother when the rotary mechanism has reached steady state.
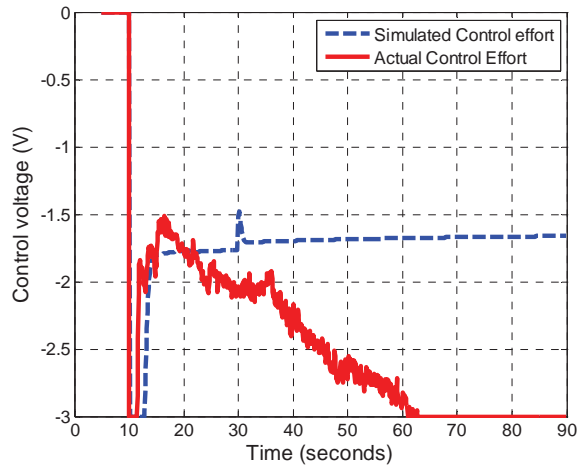
Figure 12: Voltage control effort of a PI Controller with dead zone compensation for a -700 μm targeted displacement.

11. Conclusions

A fully operational IPMC actuated rotary mechanism prototype was designed and an empirical model was developed to simulate its performance. The model was used to design a PI controller to control the position of the device. Experimental tests showed that the PI controller was effective in controlling the transient response of the rotary mechanism. Dead zone compensation was successfully implemented to keep the rotary mechanism in steady state position. It is recommended that a robust and adaptive control system is needed to manage the variable responses of the IPMC actuators.

Acknowledgements

References

[1] Shahinpoor, M. and Kim, K.J. (2001) *Ionic polymer-metal composites: I. Fundamentals.* Smart Materials and Structures. **10**(4): p. 819-833.

[2] Shahinpoor, M., Kim, K.J., and Mojarrad, M. (2007) Artificial Muscles: Applications of Advanced Polymeric Nanocomposites. New York: Taylor & Francis.

[3] Kim, K.J. (2007) Ionic Polymer-Metal Composite as a New Actuator and Transducer Material, in Electroactive polymers for robotic applications : artificial muscles and sensors, K.J. Kim and S. Tadokoro, Editors. Springer: Berlin ; London. p. 153 - 164

[4] Shahinpoor, M., Kim, K.J. and Leo, D.J. (2003) Ionic Polymer-Metal Composites as Multifunctional Materials. Polymer Composites. Vol. 24. p. 24-33.

[5] Shahinpoor, M. and Kim, K.J. (2005) Ionic polymer-metal composites: IV. Industrial and medical applications. Smart Materials and Structures. 14(1): p. 197-214.

[6] Wang, X.L., Oh, I.K. and Cheng, T.H. (2008) Mechanical Model and Analysis of ionic Polymer Metal Composites Biomimetic Actuators. Proceedings of the 7th World Congress on Intelligent Control and Automation. p. 4751-4756

[7] Manley, S.K. (2009) Performance and Feasibility of a Miniature Single Degree-of-Freedom Rotary Mechanism with Integrated IPMC Actuator. Master's Thesis in Mechanical Engineering, Auckland University.

[8] Kanno, R., Kurata, A., Tadokoro, S., Takamori, T., and Oguro, K. (1994) Characteristics and modeling of IPMC actuator. Proceedings of the Japan-USA Symposium on Flexible Automation, p. 219–225

[9] Bhat, N.D. (2003) Modeling and precision control of ionic polymer metal composite. Masters Thesis in Mechanical Engineering, Texas A&M University.

[10] Mallavarapu, K. and Leo, D.J. (2001) Feedback Control of the Bending Response of Ionic Polymer Actuators. Journal of Intelligent Material Systems and Structures. 12(3): p. 143-155.

[11] Yun, K.S. (2006) A novel three-finger IPMC gripper for microscale applications. PhD Thesis in Mechanical Engineering, Texas A&M University.